ENGINEERING APPLICATIONS OF COMPUTATIONAL FLUID MECHANICS
2026, VOL. 20, NO. 1, 2641020
https://doi.org/10.1080/19942060.2026.2641020

Taylor & Francis
Taylor & Francis Group

OPEN ACCESS Check for updates

Tip leakage vortex characteristics and phase distribution in a helico-axial multiphase pump at different flow rates

Yibo Gao[a], Linlin Geng[a], Patrick G. Verdin[b], Ibra Fall[a], Yilong Wang[a] and Desheng Zhang[a]

[a]Research Center of Fluid Machinery Engineering and Technology, Jiangsu University, Zhenjiang, People's Republic of China; [b]Faculty of Engineering and Applied Sciences, Cranfield University, Bedfordshire, UK

ABSTRACT

This study investigates tip leakage vortex (TLV) characteristics in helico-axial multiphase pumps at 20% inlet gas void fraction across three flow rates (Q/Q_{des} = 0.9, 1.0, 1.1). Numerical simulations using the SST k-ω and Eulerian-Eulerian models, validated by high-speed photography, reveal critical coupling among operating conditions, vortex dynamics, and gas–liquid phase distribution. With increasing flow rate from 0.9 to 1.1 Q_{des}, TLV penetration depth increases by 35% (measured by radial displacement), while peak vorticity intensifies from 22,500 s^{-1} to 24,500 s^{-1} at the leading edge. The vortex core migrates toward the impeller hub, with the radial position shifting from $r* = 0.990$ to $r* = 0.983$ at mid-chord, developing pronounced three-dimensional characteristics at $Q/Q_{des} = 1.1$. Vorticity concentrates at the leading edge ($\lambda = 0.15$–0.25) with peak values exceeding 24,000 s^{-1}, then decays exponentially to below 5,000 s^{-1} by mid-chord ($\lambda = 0.5$), while turbulent kinetic energy peaks at 1.5–1.6 m⊃2/s⊃2 in the mid-chord region ($\lambda = 0.4$–0.6). Gas holdup distribution exhibits strong spatial correlation with low-pressure regions, with maximum gas holdup increasing from 0.25 to over 0.4 as flow rate increases, gas volume fractions reaching 0.6–0.75 near the leading edge, and normalized gas phase deviation exceeding 300% at high flow rates, forming a coupled phenomenon where pressure depression promotes gas concentration and subsequently influences vortex structural evolution. These findings reveal TLV-induced gas accumulation is 15–20% higher than previous single-phase studies predicted, with critical implications for multiphase pump efficiency optimization.

ARTICLE HISTORY
Received 18 November 2025
Accepted 1 March 2026

KEYWORDS
Helico-axial multiphase pump; tip leakage vortex; gas-liquid two phase flow; CFD; high-speed photography

1. Introduction

Subsea hydrocarbon deposits account for approximately one-third of global petroleum reserves (Kim et al., 2014), with recent discoveries showing increasing proportions of gas-rich formations requiring advanced multiphase transportation technologies beyond conventional single-phase systems. This challenge has led to the development of multiphase transport technologies, with multiphase pumping systems serving as the core enabling technology (Liu et al., 2018a; Zhang & Tan, 2018).

These pumping systems offer significant advantages: (1) integration of production facilities through elimination of topside separation equipment and use of unified multiphase pipelines, substantially reducing infrastructure complexity and energy consumption; (2) improved reservoir recovery through reduced wellhead backpressure, enhancing extraction efficiency and maximizing hydrocarbon yield with considerable economic benefits (Zhang et al., 2015b; Zhang et al., 2016). This integrated approach represents a major advancement toward more sustainable and efficient subsea energy extraction.

Current deepwater extraction operations predominantly employ three types of multiphase pumping systems: twin-screw pumps, electrical submersible pumps, and helico-axial rotodynamic pumps. Twin-screw configurations are highly sensitive to particulate contamination, with minimal sand content causing significant wear-related performance deterioration. Electrical submersible systems show operational limitations in high gas-content environments, with stability and efficiency substantially compromised when gas fractions exceed 35% (Okafor & Verdin, 2024). In contrast, helico-axial multiphase pumps demonstrate exceptional performance stability across gas–liquid mixtures containing up to 90% gas content, making them optimal solutions for medium to high gas-oil ratio reservoirs (Suh et al., 2018). Consequently, helico-axial configurations have become the preferred technology for contemporary deepwater hydrocarbon development projects.

CONTACT Desheng Zhang zds@ujs.edu.cn Research Center of Fluid Machinery Engineering and Technology, Jiangsu University, Zhenjiang, Jiangsu, 212013, People's Republic of China

© 2026 The Author(s). Published by Informa UK Limited, trading as Taylor & Francis Group.
This is an Open Access article distributed under the terms of the Creative Commons Attribution License (http://creativecommons.org/licenses/by/4.0/), which permits unrestricted use, distribution, and reproduction in any medium, provided the original work is properly cited. The terms on which this article has been published allow the posting of the Accepted Manuscript in a repository by the author(s) or with their consent.

Helico-axial multiphase pumps represent a hybrid rotodynamic design combining operational principles from both axial-flow pumps and centrifugal compressors (Zhang et al., 2011). Operational requirements necessitate maintaining specific radial clearances between blade tips and pump casings to prevent mechanical interference. However, this design creates pressure-driven leakage pathways between blade pressure surfaces (PS) and suction surfaces (SS). The resulting tip clearance flow exhibits complex three-dimensional characteristics, ultimately developing into coherent tip leakage vortices (TLV) through interactions with mainstream flow, boundary layer effects, and relative casing motion (Liu et al., 2018b; Shi et al., 2020; Torre et al., 2011).

Tip leakage vortices introduce multiple detrimental effects: flow pattern deterioration, enhanced instability, reduced efficiency, and initiation of cavitation, rotating stall, and pressure oscillations that compromise system reliability (Gaggero et al., 2014; Mailach et al., 2001). Understanding TLV formation mechanisms and structural evolution is therefore fundamental to mitigating these adverse effects and optimizing multiphase pump performance.

Tip leakage vortex research has been a cornerstone of turbomachinery investigations since the 1950s, initiated by Rains' pioneering observations in axial-flow pumps in 1954. Rains (1954) conceptualized TLV behaviour using a gap flow jet approximation based on slender body theory, establishing early predictive frameworks for three-dimensional tip clearance flows through two-dimensional cross-flow analysis. Subsequent advances in experimental methodologies have enabled more sophisticated investigations. Wu et al. employed comprehensive two-dimensional and stereoscopic particle image velocimetry (PIV) techniques to characterize TLV structures and associated turbulence in axial water jet pumps, revealing the highly three-dimensional nature of tip region flows with pronounced chordwise variations in velocity and vorticity distributions (Wu et al., 2011a; Wu et al., 2011b; Wu et al., 2012).

Recent investigations have further elucidated TLV characteristics across various pump configurations. Zhang et al. (2015a) demonstrated that TLV inception points migrate chordwise from leading to trailing edges with increasing flow rates in axial pump configurations. Liu and Tan (2019) investigated TLV characteristics in mixed-flow pumps through SST k-ω turbulence modelling. Their analysis revealed that TLV spatial–temporal evolution within a single impeller revolution follows three distinct stages: splitting, developing, and merging. The study demonstrated that TLV oscillations are intensified by sudden pressure variations at blade junctions, with relative vortex stretching identified as the primary mechanism driving TLV splitting and shedding. Shi et al. (2020) characterized TLV trajectories as exhibiting sinusoidal distributions with rotational intensities directly proportional to blade pressure differentials, while identifying dual low-pressure regions within tip clearances: pressure-side separation vortices and suction-side tip leakage vortices. Advanced studies have revealed the cyclical nature of TLV behaviour within single impeller rotations, involving dynamic splitting-dissipation-regeneration processes (Shi et al., 2024).

Recent advances in vortex dynamics theory have provided deeper insights into TLV evolution mechanisms in multiphase pumps. Zhou et al. (2025) proposed a Reynolds-averaged transport equation for the enstrophy of rigid vorticity in gas–liquid two-phase flow, systematically analyzing energy loss mechanisms caused by tip clearance leakage vortex generation and dissipation. Their analysis revealed that rigid vorticity evolution in the main flow passage is dominated by the Coriolis Force Term, while shear vorticity generation is controlled by the Vorticity Stretching Term, and the Baroclinic Torque Term couples with gas–liquid density gradients to influence vortex structure. Building on this theoretical framework, Zhang et al. (2025) investigated the flow characteristics of tip clearance leakage in spiral axial-flow multiphase pumps using the Q-criterion vortex identification method, identifying three typical vortex structures: separation vortex, gap leakage vortex, and blade passage vortex, with each structure governed by distinct dynamic mechanisms.

The relationship between TLV and pressure pulsation has been systematically examined across different operational regimes. Jia et al. (2025) analyzed TLV behaviour under optimal, critical stall, and deep stall conditions in axial flow pumps designed for underwater vehicles, demonstrating that the compression-expansion term dictates TLV core strength while viscous dissipation determines pressure pulsation frequency. Shi et al. (2024) further investigated TLV dynamic characteristics in oil-gas multiphase pumps through vorticity decomposition theory, revealing that gas phase presence significantly enhances TLV scale and strength while prolonging its existence in the flow channel, with the Rigid vorticity Curl of pseudo-Lamb vector Term (RCT) playing a crucial role under gas–liquid two-phase conditions. The gas–liquid separation phenomenon represents another critical aspect of multiphase pump performance. Quan et al. (2024) investigated gas–liquid separation characteristics in helico-axial multiphase pumps, identifying that separation occurs near 2/3 of the airfoil bone line, with gas blockage phenomena resulting in significant energy losses in compression units.

While substantial research has characterized tip leakage vortex phenomena in single-phase flows, comprehensive understanding of TLV behaviour in multiphase environments remains limited. Previous investigations have primarily examined overall pump performance or single-phase TLV characteristics, with insufficient attention to the coupling mechanisms between vortex dynamics and phase redistribution in gas–liquid flows. Specifically, the fundamental mechanisms governing TLV structural evolution under varying flow conditions and their coupling with gas–liquid phase distribution require systematic investigation. This knowledge gap is particularly critical for helico-axial multiphase pumps operating across wide flow rate ranges with significant gas content variations.

This study addresses these gaps through detailed examination of TLV formation mechanisms, governing parameters, spatial configurations, and fluid dynamic characteristics across different operational flow rates, with particular emphasis on off-design conditions and multiphase flow effects on TLV development. The investigation employs advanced computational fluid dynamics (CFD) methodology utilizing the SST k-ω turbulence model, implemented through ANSYS Fluent to simulate a multi-stage helico-axial multiphase pump configuration with 0.5 mm tip clearance across three distinct operational flow rates: $Q/Q_{des} = 0.9$, 1.0, and 1.1, where Q_{des} represents the design flow rate. Numerical methodology validation is achieved through comparison with experimental flow field data obtained via high-speed imaging techniques. Distinguished from previous studies, this work provides systematic quantification of TLV characteristics across three flow rate conditions with experimental validation, and comprehensively reveals the unique coupling between pressure-induced gas accumulation and vortex structural modification in multiphase flows. The primary research objectives include: (1) investigating correlations between TLV rotational intensity and blade pressure differentials under varying flow rate conditions; (2) systematically analyzing tip clearance velocity distributions to elucidate fundamental TLV structural evolution mechanisms; (3) characterizing gas–liquid phase distribution patterns within TLV structures and their coupling with vortex dynamics. These research findings will provide valuable insights for advancing tip clearance studies in helico-axial gas–liquid multiphase pumps. This investigation focuses on a representative operational envelope – flow rates of 0.9–1.1 Q_{des} at 20% inlet gas void fraction – typical of offshore subsea boosting applications where TLV effects are most critical. The analysis framework enables extension to geometrically similar helico-axial pumps of different scales, while the fundamental mechanisms identified provide insights transferable to broader multiphase turbomachinery applications.

2. Methodology

2.1. Experimental setup

2.1.1. Test facility description

Experiments were conducted on a closed-loop multiphase pump test facility at the Zhenjiang Fluid Engineering Equipment Technology Research Institute, Jiangsu University (Figure 1). The facility uses transparent Perspex construction to enable optical flow visualization. The pump model, with a clear casing, is mounted horizontally to facilitate high-speed imaging and internal flow observation.

The experimental loop comprises three primary circulation systems: gas supply, liquid circulation, and mixed-phase transport networks. The liquid circulation system uses a multi-functional storage tank as the water source, with flow rate controlled by electromagnetic flowmeters. An air compressor provides the gas supply, with flow regulation achieved through electronically controlled valves. A downstream pressure stabilization vessel dampens sudden pressure transients and provides supplementary liquid during temporary pressure reductions. A non-return valve in the gas supply line prevents liquid backflow and protects the compression equipment.

Air and water are mixed in a specially designed mixing tank before entering the pump, ensuring uniform gas–liquid distribution at the inlet. When the gas–liquid mixture flows through the pump during tests, air escapes to atmosphere while water returns to the storage tank, forming a closed-loop circulation.

2.1.2. Measurement and visualization system

The facility is equipped with comprehensive measurement and visualization systems to monitor pump performance and flow characteristics. Pressure sensors are installed at the inlet and outlet sections to measure pressure rise across the pump. Temperature sensors record fluid temperature variations during operation. Electromagnetic flowmeters measure liquid and gas flow rates with high precision. The data acquisition system records parameter changes at various measurement points in real-time, providing data for subsequent analysis. All sensors were calibrated according to manufacturer specifications before testing.

The high-speed visualization system (Figure 2) comprises a digital camera (Revealer S1315M/C), macro optics, a 750 W continuous halogen lamp, and an image processing computer. The camera operates at

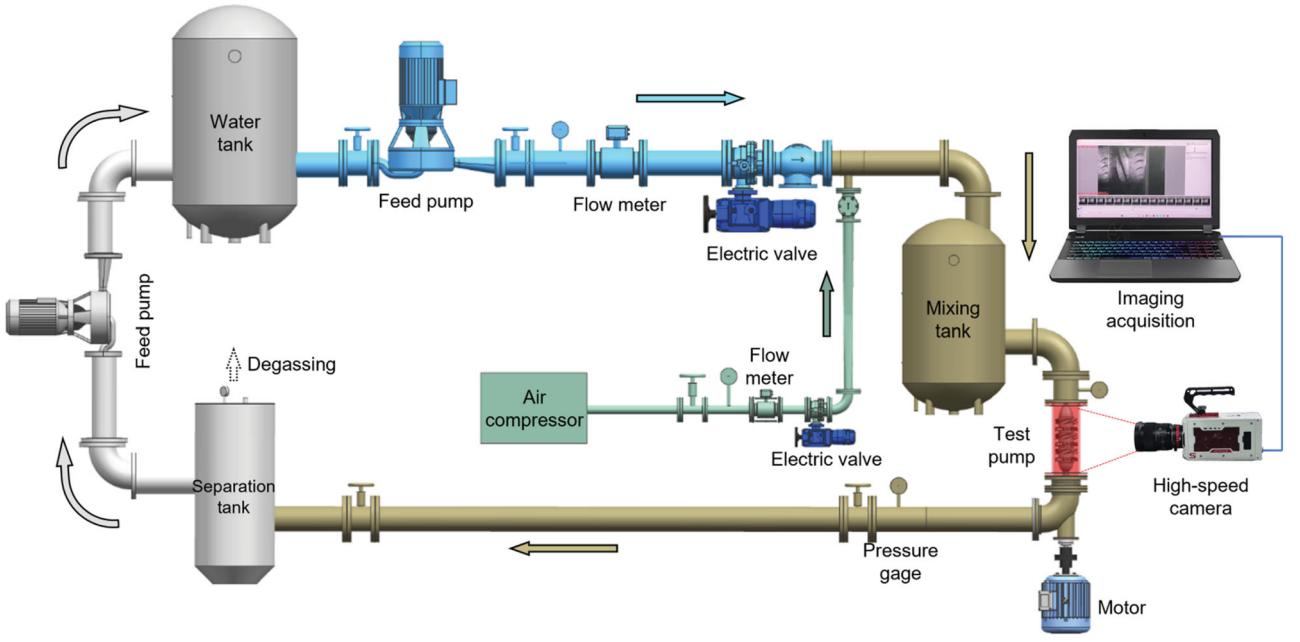

Figure 1. Schematics of the axial flow multiphase pump loop.

a sampling frequency of 10,000 Hz with an exposure time of 5 μs to capture rapid flow phenomena in the blade tip region. Camera calibration was performed using reference images positioned on the casing observation area. After initial calibration, focus and exposure parameters were adjusted to obtain clear bubble images in the blade tip region. The high-intensity halogen lamp provides sufficient illumination for high-frequency image capture. Discrete bubbles within the gas–liquid mixture serve as natural flow tracers, enabling TLV trajectory visualization and validation of numerical predictions. The image processing computer acquires and stores the high-speed images for post-processing analysis.

2.1.3. Experimental uncertainty analysis

The total experimental uncertainty consists of systematic uncertainty $E_{\eta S}$ and random measurement uncertainty $E_{\eta R}$. Systematic uncertainty follows a deterministic pattern without compensating characteristics and is primarily determined by instrument accuracy. According to international standard ISO 9906, the systematic uncertainty of pump efficiency comprises individual systematic uncertainties as expressed in the following equation:

$$E_{\eta S} = \sqrt{E_{QlS}^2 + E_{QgS}^2 + E_{MS}^2 + E_{nS}^2} \tag{1}$$

where E_{QlS} is the systematic uncertainty of liquid flow rate measurement, E_{QgS} is the systematic uncertainty of gas flow rate measurement, E_{MS} is the systematic uncertainty of torque measurement, and E_{nS} is the systematic uncertainty of rotational speed measurement.

Random measurement uncertainty follows statistical laws and exhibits compensating characteristics. It is commonly processed using probabilistic statistical methods, with errors following a t-distribution. The standard deviation is given by:

$$S_x = \sqrt{\frac{1}{n-1}\left[\sum_{i=1}^{n}(x_i - \bar{x})^2\right]} \tag{2}$$

where S_x is the standard deviation, x_i represents individual measurements, $\bar{x}$is the arithmetic mean of measurements, and n is the number of measurements.

$$E_{\eta R} = \pm\sqrt{E_{QlR}^2 + E_{Q_gR}^2 + E_{MR}^2 + E_{nR}^2} \tag{3}$$

where E_{QlR} is the random uncertainty of liquid flow rate measurement, E_{QgR} is the random uncertainty of gas flow rate measurement, E_{MR} is the random uncertainty of torque measurement, and E_{nR} is the random uncertainty of rotational speed measurement.

Seven repeated tests were conducted at the design volumetric flow rate with inlet gas void fraction IGVF = 20%. The mean values and standard deviations were calculated from the measurement data, with specific parameters shown in Table 1. Among the four measurement parameters, gas flow rate measurement exhibited the highest combined uncertainty of 2.85%, with a standard deviation of 2.88%, indicating relatively poor repeatability and serving as the primary factor affecting overall experimental uncertainty. Torque measurement showed a combined uncertainty of 1.14%, with systematic uncertainty (1.10%) slightly higher than random uncertainty

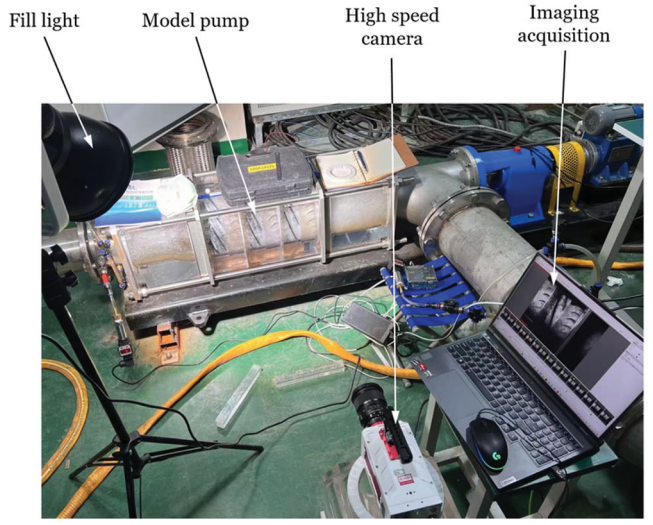

(a) High-speed imaging system setup

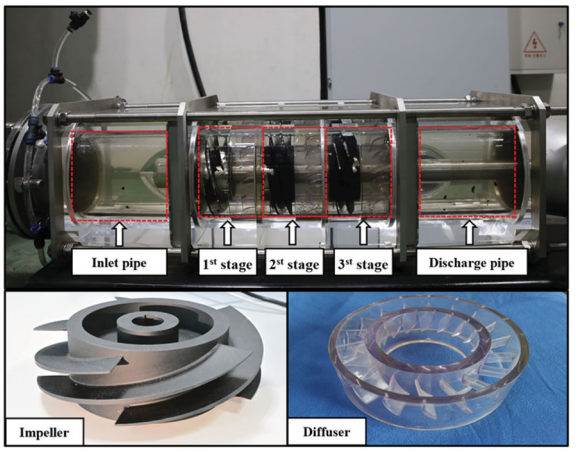

(b) Visualization of hydraulic components

Figure 2. Experimental setup for TLV trajectory visualization.

Table 1. Experimental Uncertainty Calculation.

Measurement No.	Q_l(m^3/h)	Q_g(Nm^3/h)	T(N·m)	n(r/min)
1	105	27.1	19.68	1300
2	107	26.9	19.36	1300
3	105	24.9	19.85	1300
4	106	25.7	19.74	1301
5	106	26.2	19.37	1302
6	105	26.4	19.25	1300
7	104	25.8	19.37	1301
Mean	105.42	26.14	19.51	1300.57
Standard Deviation (%)	0.92	2.88	1.19	0.06
Standard Deviation (%)	0.85	2.67	1.10	0.05
Random Uncertainty (%)	0.50	1.00	0.30	0.10
Combined Uncertainty U_{com} (%)	0.99	2.85	1.14	0.12
Total Uncertainty U_{all} (%)	3.23			

(0.30%), suggesting that torque measurement accuracy is primarily limited by instrument precision. Liquid flow rate and rotational speed measurements demonstrated relatively low combined uncertainties of 0.99% and 0.12%, respectively. Rotational speed measurement exhibited the lowest uncertainty with a standard deviation of only 0.06%, indicating excellent stability of the speed control and measurement system. The total uncertainty of 3.23% complies with ISO 9906 requirements for pump performance testing ($\leq 5\%$), confirming that the measurement accuracy and data reliability of this experimental system meet research requirements.

2.2. Numerical setup

2.2.1. Governing equations

The gas–liquid multiphase flow was modelled using the Eulerian-Eulerian approach. The conservation equations were derived by ensemble averaging the instantaneous local balance for each phase (Drew & Passman, 1999; Ishii & Hibiki, 2010). The governing equations for continuum and momentum can be given as

$$\frac{\partial}{\partial t}(\alpha_i \rho_i) + \nabla \cdot (\alpha_i \rho_i \bar{\boldsymbol{u}}_i) = 0 \tag{4}$$

$$\frac{\partial(\alpha_i \rho_i \bar{\boldsymbol{u}}_i)}{\partial t} + \nabla \cdot (\alpha_i \rho_i \bar{\boldsymbol{u}}_i \bar{\boldsymbol{u}}_i) = -\alpha_i \nabla P + \nabla \cdot (\overline{\overline{\tau_i}}) + \alpha_i \rho_i \boldsymbol{g} + \boldsymbol{F}_{i,j} \tag{5}$$

In the above equations, the subscript i denotes the phase index, with α, ρ and $\boldsymbol{u}_i$ represent the volume fraction, density and resolved velocity, respectively. P denotes the pressure, and $\overline{\overline{\tau_i}}$ represents the phase stress–strain tensor. $\boldsymbol{F}_{i,j}$ denotes the interfacial forces responsible for momentum transfer between phases, including drag, lift, and virtual mass forces. Drag force constitutes the primary mechanism of momentum coupling between continuous and discrete phases. For bubbly flow in multiphase pumps, drag was considered as the dominant interphase force, while the influence of other interphase forces was neglected in this study. The equation is as follows:

$$\boldsymbol{F}_D = -\frac{3}{4}\alpha_i \alpha_j \rho_j \frac{C_D}{d_b} |\boldsymbol{v}_r| \boldsymbol{v}_r \tag{6}$$

where $\boldsymbol{v}_r$ represents relative velocity, C_D represents the drag coefficient which depends on the selected drag model. The Schiller-Naumann model was adopted to calculate the drag coefficient, as expressed by:

$$C_D = \begin{cases} \dfrac{24}{Re_b}(1 + 0.15 Re_b^{0.687}) & Re_b \leq 1000 \\ 0.44 & Re_b > 1000 \end{cases} \tag{7}$$

where Re_b represents the Bubble Reynolds number (Schiller & Naumann, 1933)

$$Re_b = \frac{\rho_i d_b |\boldsymbol{u}_g - \boldsymbol{u}_l|}{\mu_i} \tag{8}$$

The SST k-ω turbulence model was employed for simulating the bubbly flow. This model combines the robustness and accuracy of the k-ω formulation in near-wall regions with the free-stream independence of the k-ε formulation. The SST k-ω turbulence model consists of two transport equations for the turbulent kinetic energy k and the specific dissipation rate ω.

$$\frac{\partial(\rho_i k)}{\partial t} + \frac{\partial}{\partial x_j}(\rho_i \bar{\boldsymbol{u}}_j k) = \frac{\partial}{\partial x_j}\left[\left(\mu + \frac{\mu_t}{\sigma_k}\right)\frac{\partial k}{\partial x_j}\right] + P_k - \beta^* \rho_i k\omega + P_\omega + \Pi_{kq} \tag{9}$$

$$\frac{\partial(\rho_i \omega)}{\partial t} + \frac{\partial}{\partial x_j}(\rho_i \bar{\boldsymbol{u}}_j \omega) = \frac{\partial}{\partial x_j}\left[\left(\mu + \frac{\mu_t}{\sigma_\omega}\right)\frac{\partial \omega}{\partial x_j}\right] + a\frac{\omega}{k}P_k - \beta\rho_i\omega^2 + (1 - F_1)2\rho_i \frac{1}{\sigma_{\omega 2}\omega}\frac{\partial k}{\partial x_j}\frac{\partial \omega}{\partial x_j} + \Pi_{\omega q} \tag{10}$$

where P_k denotes the production term of turbulent kinetic energy, μ_t represents the turbulent eddy viscosity, F_1 is the blending function, and α, β^*, β, σ_k and σ_ω are model coefficients (Menter, 1994). The turbulent viscosity is defined as:

$$\mu_t = \frac{\rho a_1 k}{\max(a_1\omega, SF_2)} \tag{11}$$

where $a_1 = 0.31$, F_2 is a blending function that restricts the limiter to the wall boundary layer, S is an invariant measure of the strain rate.

The dispersed turbulence model was selected to account for turbulence modulation within the Eulerian-Eulerian framework. This approach captures the influence of bubbles on the continuous phase turbulence characteristics while maintaining a balance between computational efficiency and numerical accuracy.

2.2.2. Geometric model and mesh generation

A sliding mesh approach was implemented for TLV analysis. The computational domain comprised an inlet section, a three-stage impeller-diffuser assembly, and a discharge section (Figure 3a). The domain was partitioned into eight distinct regions, where the impeller section (including tip clearance) was designated as the rotating zone and the guide vane diffuser as the stationary zone. Sliding interfaces were applied at the impeller boundaries. Table 2 presents the main design and operational parameters of the multiphase pump used in this study.

A structured hexahedral mesh generated using TurboGrid 20.2 was employed throughout the computational domain to minimize truncation error and enhance convergence characteristics (Figure 3b). The 0.5 mm tip clearance region incorporated 20 grid nodes to ensure adequate resolution of leakage flows and vortical structures (Figure 4a). Progressive mesh refinement near the tip region was implemented to maintain solution accuracy while optimizing computational cost. The boundary layer mesh was constructed such that the non-dimensional wall distance maintained $y^+ < 1$, as required by the wall treatment of the SST k-ω turbulence model (Figure 4b).

2.2.3. Simulation settings

ANSYS Fluent was used to solve the three-dimensional Reynolds-averaged Navier-Stokes (RANS) equations and conduct numerical simulations of the multiphase pump. The Eulerian-Eulerian multiphase flow model was adopted to capture the complex gas–liquid flow phenomena. As mentioned previously, the SST k-ω two-equation turbulence model was employed. Previous studies have demonstrated the superior performance of this model in predicting turbulent flow details for similar applications (Shi et al., 2019; Tang et al., 2018). The high-speed rotation of the impeller enhances turbulence intensity in the circumferential direction, while blades and diffuser vanes experience significant wall shear. Additionally, flow destabilization phenomena such as stall can substantially increase turbulence intensity.

The inlet boundary condition was specified as a mass-flow inlet with a gas volume fraction of 20%, while the outlet was set as a pressure outlet. All wall surfaces were treated with no-slip boundary conditions to capture boundary layer effects and wall shear interactions. The interface between rotating and stationary domains was modelled using transient rotor-stator interface conditions to account for the relative motion between impeller and diffuser components.

A fully implicit coupling algorithm was employed in the numerical simulations. Steady-state simulations were first performed under different operating conditions, followed by transient simulations initialized from the steady-state solutions. The Schiller-Naumann drag model was employed to describe interphase momentum transfer. The impeller speed was set to 1300 rpm. The SIMPLEC algorithm was used for pressure-velocity coupling, and a second-order upwind scheme was applied for convection term discretization to ensure computational accuracy. For steady-state simulations, the convergence

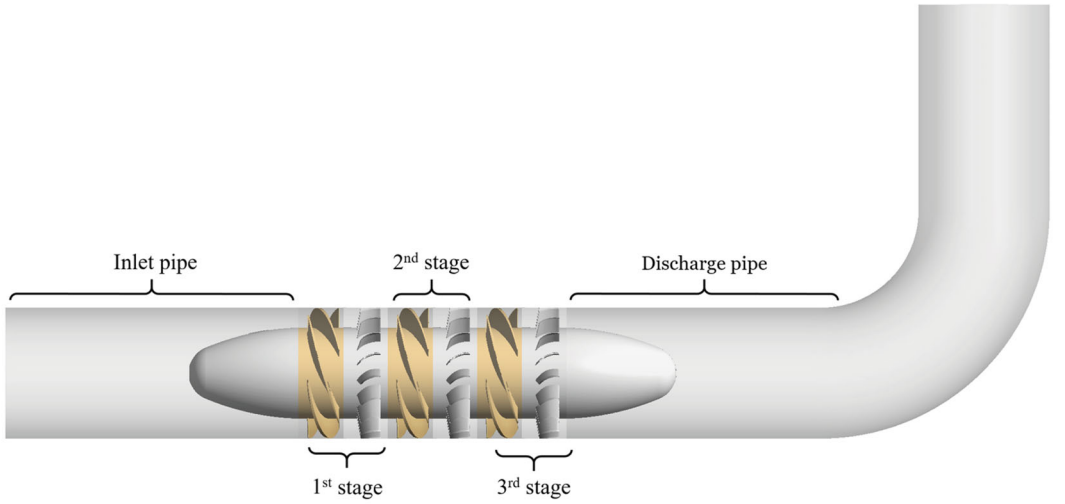

(a) Schematic diagram of the helico-axial multiphase pump model

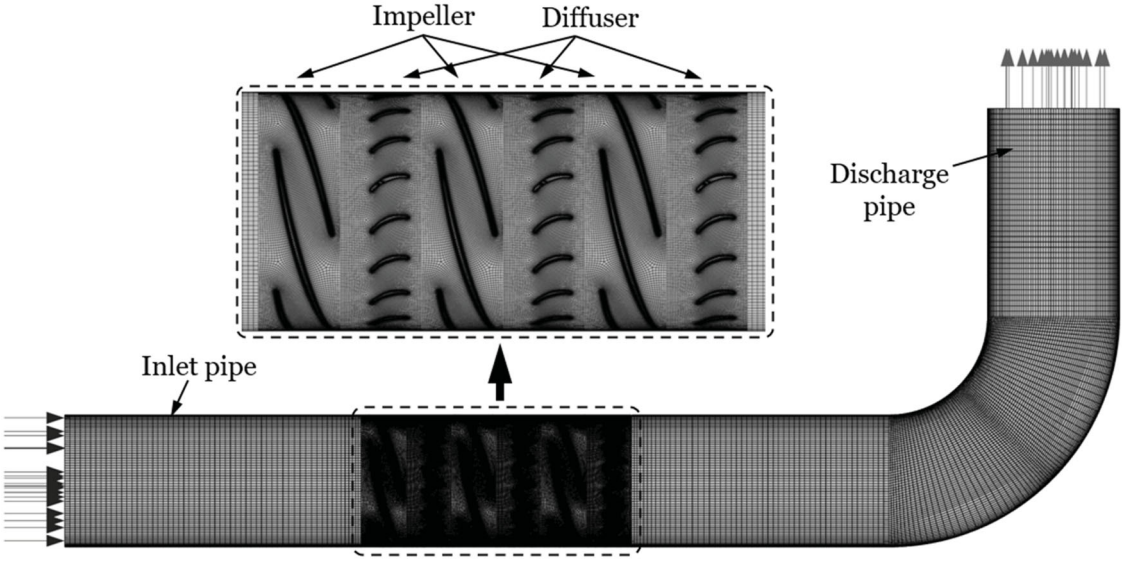

(b) Calculation domain mesh.

Figure 3. Computational configuration of multiphase pump

criterion was set to a maximum residual of 10^{-4} with a maximum of 2000 iterations. For transient simulations, a time step of 0.000256 s (corresponding to 2° of impeller rotation) was employed, with a total simulation time of 0.6912 s and a maximum of 20 iterations per time step. The specific settings of the boundary conditions are listed in Table 3. The simulation was conducted for 15 impeller revolutions. To obtain accurate time-averaged results, data from the last 5 revolutions were used for statistical averaging.

The three operating conditions were selected to represent typical operational scenarios in offshore multiphase pumping systems: $Q/Q_{des} = 1.0$ corresponds to design conditions, $Q/Q_{des} = 0.9$ represents part-load operation during reservoir pressure decline, and $Q/Q_{des} = 1.1$ captures overload conditions during peak production

Table 2. Main parameters of multiphase pump.

Parameter	Value
Design Flow Rate/(m³/h)	130
Rotating Speed/(rpm)	1300
Impeller Outer Diameter/(mm)	200
Tip clearance/(mm)	0.5
Impeller Blade Count	5
Diffuser Blade Count	18

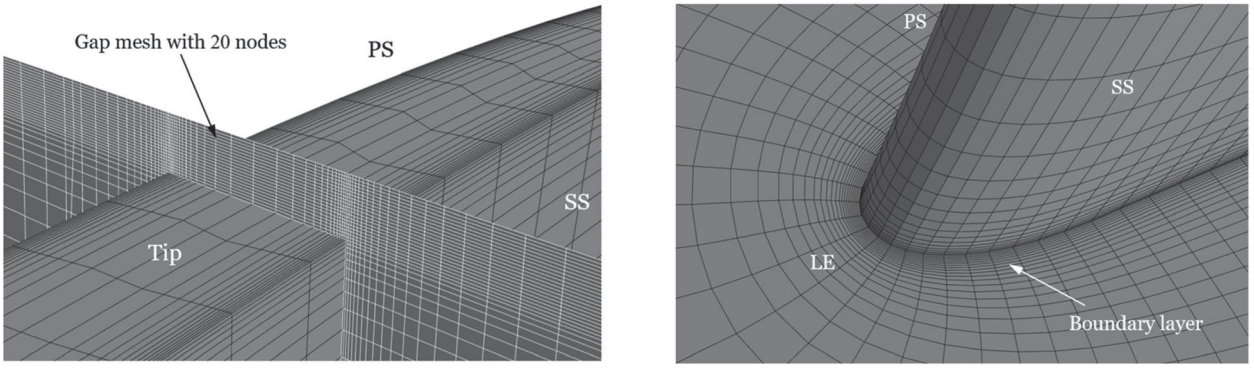

(a) Refined mesh near tip (b) Mesh near the blade surface

Figure 4. Mesh of the multiphase pump.

Table 3. Numerical simulation setup.

Item	Setting
Multiphase flow model	Eulerian-Eulerian
Turbulence model	SST *k-ω*
Drag force model	Schiller-Naumann
Inlet boundary	Mass-flow Inlet
Outlet boundary	Pressure Outlet
Wall condition	No-slip Wall
Impeller speed	1300 r/min
Inlet gas volume fraction	20%
Interface condition	Transient Rotor
P-V coupling algorithm	SIMPLEC
Convection term discretization	Second-order
Maximum residual value	10^{-4}
Time step	0.000256s (2°)
Total calculation time	0.6912s
Maximum number of iterations	20 (each time step)

demands. This flow rate range ($0.9–1.1Q_{des}$) encompasses the majority of operational time in field applications and is critical for understanding pump performance degradation mechanisms across realistic operating envelopes. Measurement locations at the blade tip clearance, vortex core centres, and multiple axial sections enable systematic tracking of TLV structural evolution from formation through dissipation, which directly correlates with hydraulic efficiency losses and operational stability in deepwater extraction systems.

2.2.4. Mesh independence test and experimental validation

Grid independence was verified using the Richardson Extrapolation method with the Grid Convergence Index (GCI) criterion (Celik et al., 2008) across three systematically refined meshes. Details of the fine, medium, and coarse meshes are provided in Table 4. The GCI values for head rise were 0.623% and 3.57% for the fine and medium meshes, respectively. Based on the balance between computational efficiency and numerical accuracy, the medium mesh (16.03 million cells) was selected for subsequent simulations.

Table 4. The results of mesh convergence verification.

Mesh	Cell	φ_k(kPa)	Approximate error e_a(%)	Extrapolated error e_{ext}(%)	GCI(%)
Fine	26.42 M	63.08	9.49%	2.52%	3.57%
Medium	16.03 M	69.69	1.86%	0.504%	0.623%
Coarse	6.52 M	68.42			

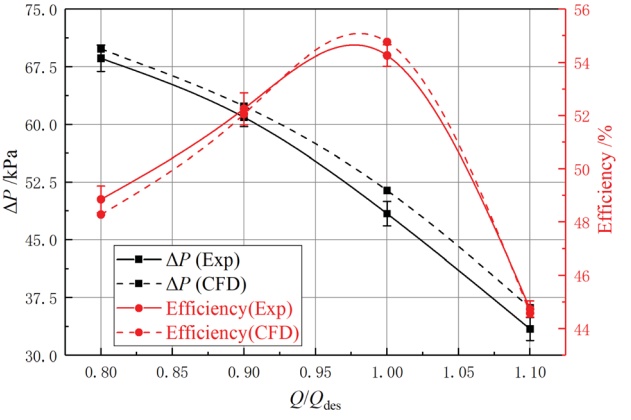

Figure 5. Comparison of external characteristic between numerical simulation results and test results.

To validate the numerical model, computed results were systematically compared with experimental measurements. Figure 5 presents quantitative comparison of pump external characteristics between numerical predictions and experimental data. For pressure rise, the numerical model achieves excellent accuracy with maximum deviations below 5% across the entire flow rate range. The mean absolute percentage error (MAPE) for pressure rise is 3.2%. Efficiency predictions demonstrate satisfactory accuracy with MAPE of 4.8%, successfully capturing both the characteristic curve trend and peak efficiency location at $Q/Q_{des} = 1.0$. The slightly higher deviation in efficiency at off-design conditions ($Q/Q_{des} = 0.9$ and 1.1) is attributed to increased flow

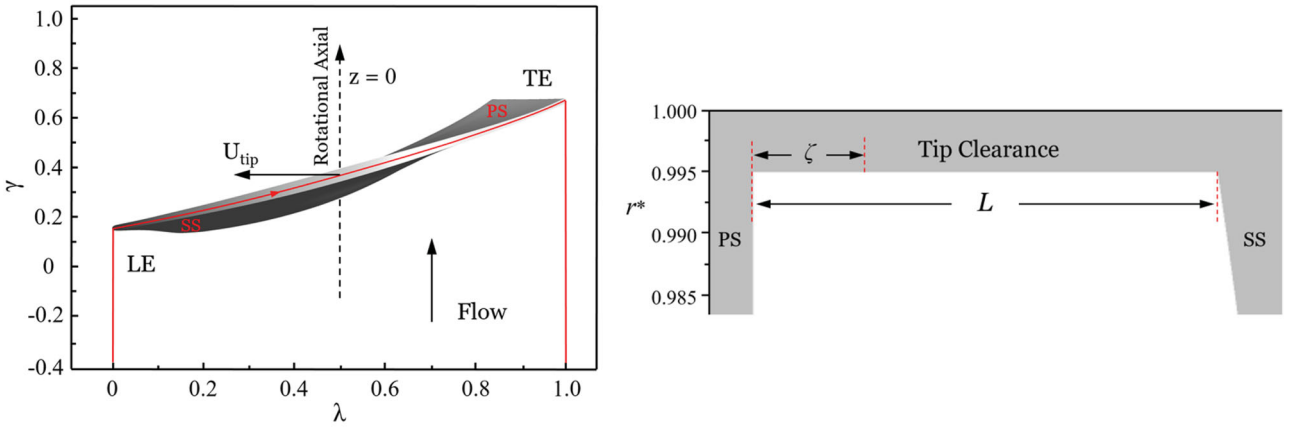

(a) Blade chord fraction λ

(b) Blade thickness fraction ζL^{-1}

Figure 6. Blade tip parameters definition.

separation and secondary flow complexity that are inherently more challenging to predict with RANS turbulence models, consistent with findings reported by Suh et al. (2018) for similar multiphase pump configurations.

3. Results and discussion

3.1. Tlv trajectory and flow patterns

To investigate TLV trajectory evolution, a blade-fitted coordinate system is established. Figure 6 illustrates the coordinate system used for the blade tip analysis, where the chord fraction λ represents the normalized position along the blade from leading edge ($\lambda = 0$) to trailing edge ($\lambda = 1$). The blade axial coefficient $\gamma = 2Z_{imp}/D_r$ characterizes the axial position, where Z_{imp} is the impeller axial distance and D_r is the impeller diameter. Within the blade tip clearance region (Figure 6b), the thickness fraction ζL^{-1} describes the position from the pressure surface, where ζ is the distance from the pressure surface and L is the tip thickness. The dimensionless radial location $r* = 2r/D_c$ enables systematic tracking of TLV development along the blade surface, where r is the radius of the impeller and D_c is the diameter of the casing. This coordinate system facilitates quantitative analysis of vortex core migration patterns and their correlation with local flow conditions.

Figure 7 presents a comparison between numerical simulation results and experimental observations of TLV structures under three different flow rate conditions. The left column shows the numerical results visualized using Q-criterion iso-surfaces ($Q = 3\times10^4$), the right column displays the corresponding experimental flow visualization images. Three operating conditions are examined: $Q/Q_{des} = 0.9$, 1.0, and 1.1. The numerical simulations successfully capture the primary characteristics of the TLV development observed in the experiments. At $Q/Q_{des} = 0.9$, the TLV appears relatively compact and concentrated near the blade tip region. As the flow rate increases to $Q/Q_{des} = 1.0$, the vortex structure becomes more elongated and extends further downstream. At $Q/Q_{des} = 1.1$, the TLV shows increased intensity and complexity, with more pronounced three-dimensional characteristics. Additionally, it can be observed that with increasing flow rate, the tip leakage vortex gradually migrates toward the suction side of the blade, indicating a shift in the vortex trajectory due to the enhanced mainstream flow momentum and altered pressure distribution across the blade tip clearance. The good qualitative agreement between numerical predictions and experimental observations validates the capability of the CFD model to accurately simulate TLV behaviour across different operating conditions.

Figure 8 illustrates the distribution of TLV vortex core trajectories in two different coordinate planes under three operating conditions ($Q/Q_{des} = 0.9$, 1.0, and 1.1). Figure 8(a) shows the trajectory in the r∗-λ plane (radial position versus blade chord fraction), while Figure 8(b) presents the trajectory in the γ-λ plane (axial coefficient versus blade chord fraction). These figures provide a precise visualization of the tip leakage vortex trajectories, clearly revealing the distinct differences in vortex inception points under different flow rate conditions.

In the r∗-λ plane, the TLV core trajectories exhibit distinct patterns depending on the flow rate. The differences in starting points of the tip leakage vortex under various flow conditions are evident from the figure. At all operating conditions, the vortex core initially forms near the tip clearance region (r∗ $\approx$ 0.995) and gradually moves inward as it progresses along the blade chord. The

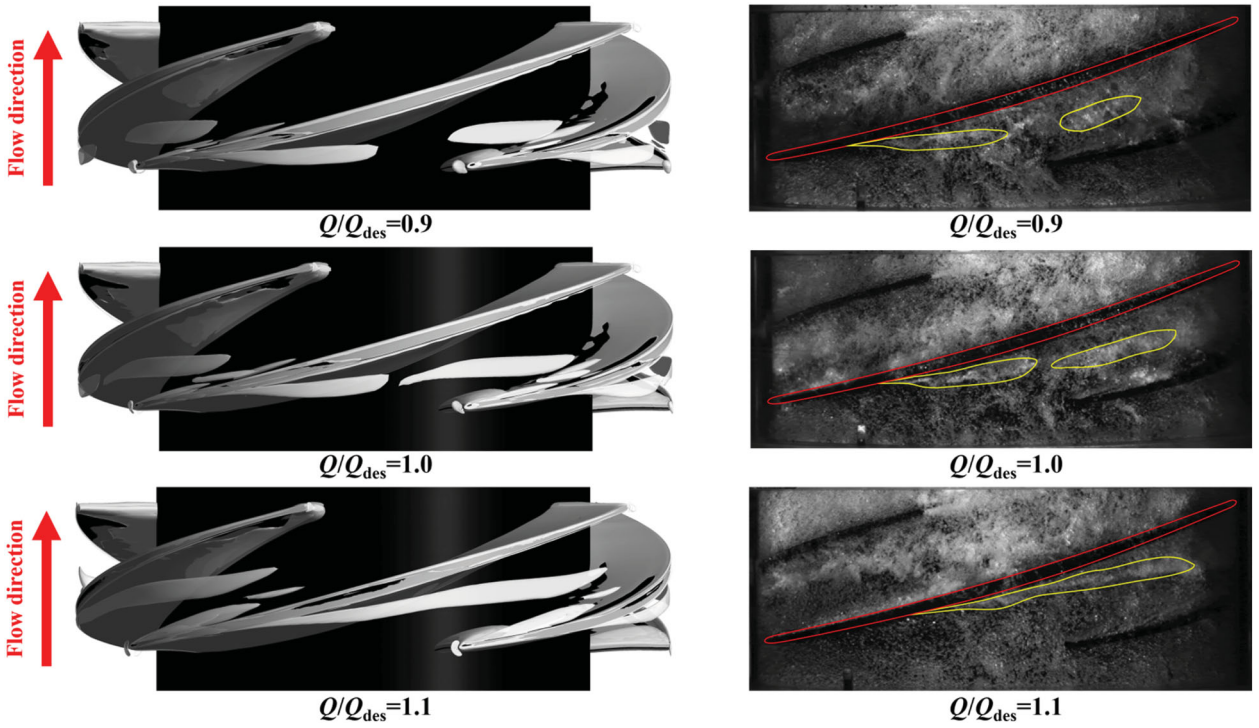

Figure 7. Comparison of numerical and experimental TLV visualization at three flow rates (Q/Q_{des} = 0.9, 1.0, 1.1). Left: CFD results using Q-criterion iso-surfaces ($Q = 3\times10^4$); Right: high-speed photography.

upper plot demonstrates that as flow rate increases, the tip leakage vortex trajectory extends inward for a longer distance. The trajectory shows a characteristic dip around λ = 0.4–0.5, indicating the vortex core migration toward the blade hub. Notably, the return behaviour observed at λ = 0.4 in both the 0.9 and 1.0 operating conditions shows a reduced degree of return in the 1.1 operating condition. At Q/Q_{des} = 1.1, the vortex core penetrates deeper into the main flow channel, reaching lower r∗ values compared to part-load and design conditions.

The γ-λ plane reveals the axial development of the TLV core. All trajectories originate from the pressure surface (PS) region and progress toward the suction surface (SS) as the flow moves downstream. The trajectories show a nearly linear trend with increasing slope toward the trailing edge. The overload condition demonstrates the most pronounced axial displacement, with the vortex core extending further in the axial direction compared to lower flow rates.

Figure 9 presents three-dimensional streamline distribution in the tip clearance region. A distinctive recirculation phenomenon occurs where leakage flow from the leading edge initially moves toward the pressure surface before returning to the suction side, with this recirculation zone extending progressively longer at higher flow rates. Within the tip clearance region, several distinct flow phenomena can be identified. The primary leakage flow moves from the pressure side to the suction side, driven by the pressure differential across the blade tip. This recirculation zone extends progressively longer at higher flow rates, demonstrating the enhanced complexity of the flow field under overload conditions.

The velocity distribution shows significant variations across operating conditions. High-velocity regions are predominantly concentrated near the leading edge and mid-chord regions where the pressure gradient is steepest. At Q/Q_{des} = 1.1, the maximum velocities increase substantially, indicating intensified tip leakage flow. The streamline trajectories exhibit increasing complexity with higher flow rates. At Q/Q_{des} = 0.9, streamlines follow relatively orderly paths with minimal cross-flow interactions. As flow rate increases, the streamlines show more pronounced three-dimensional characteristics, with increased mixing between the tip leakage flow and the main passage flow.

The interaction between adjacent streamlines reveals the vorticity generation mechanism. The shear between high-velocity tip leakage flow and the relatively slower main passage flow creates the rotational motion that forms the tip leakage vortex. This shear intensity increases markedly at higher flow rates. Near the blade tip surface, the streamlines show boundary layer separation characteristics, particularly at the trailing edge region where adverse pressure gradients are most pronounced.

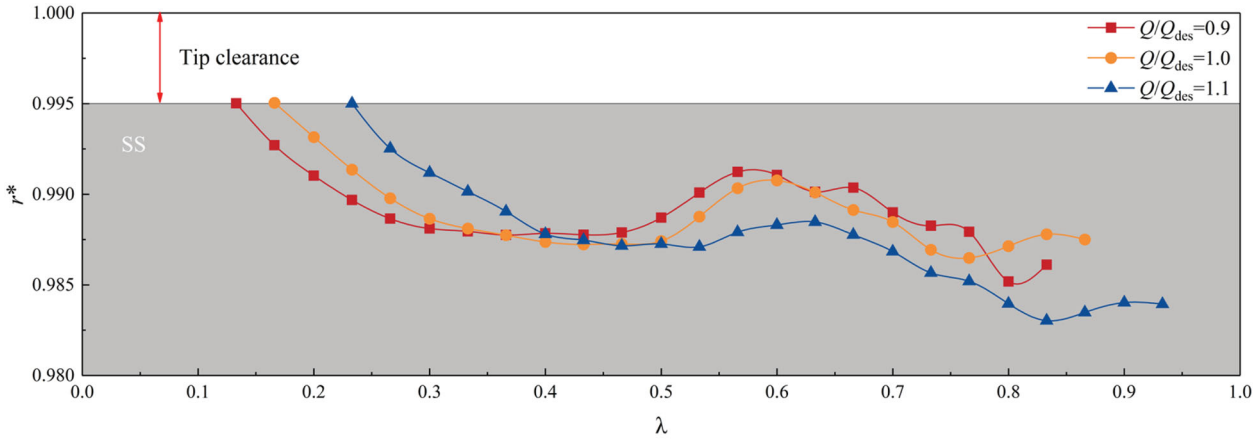

(a) r*-λ plane

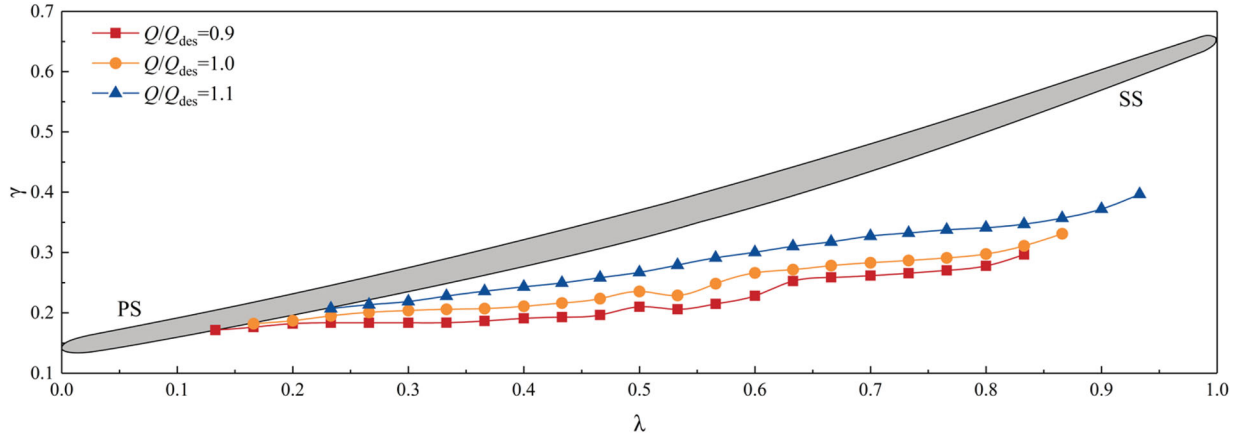

(b) γ-λ plane

Figure 8. TLV vortex core trajectories at different flow rates. (a) radial position (r) versus chord fraction (λ); (b) axial coefficient (γ) versus chord fraction (λ).

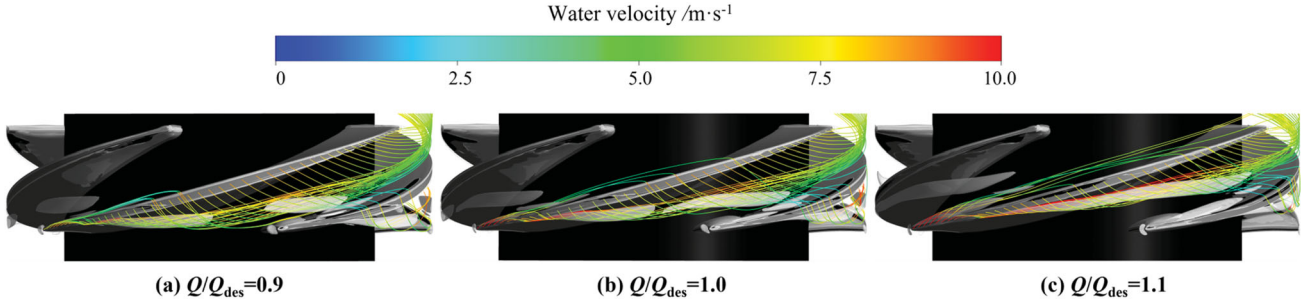

Figure 9. Three-dimensional streamline distribution of tip clearance under different flow rate conditions.

Figure 10 presents absolute velocity distribution near the tip clearance region (r∗ = 0.99). The velocity patterns directly correlate with the TLV characteristics previously identified. At $Q/Q_{des} = 0.9$, the velocity field shows uniform distribution with moderate gradients. High velocities concentrate near the leading and mid-chord edges where pressure differentials are greatest, explaining the compact TLV structure in Figure 7.

As the flow rate increases to $Q/Q_{des} = 1.0$, the velocity magnitude exhibits significant amplification, particularly in the central blade passage region. The velocity contours

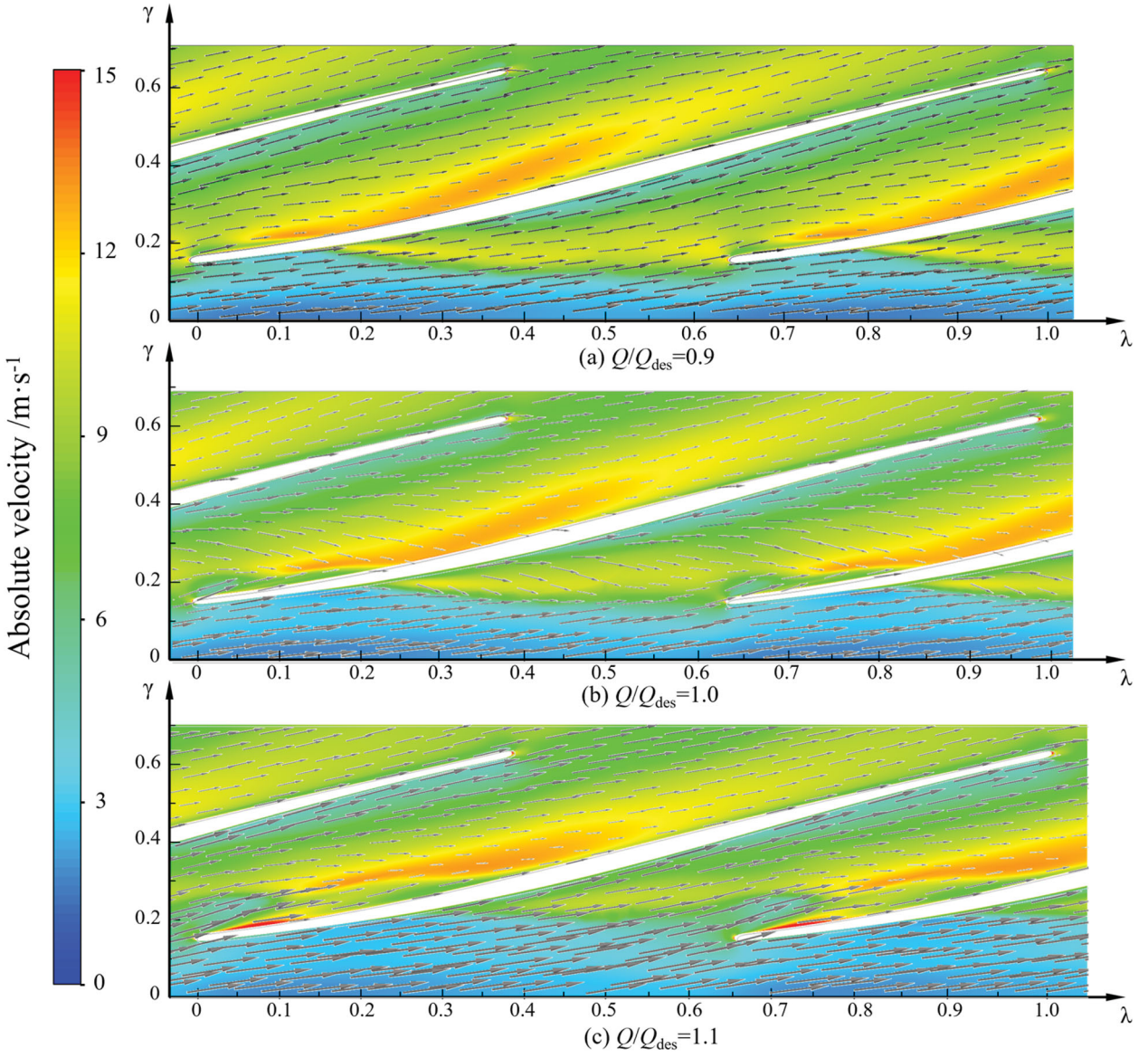

Figure 10. Absolute velocity distribution near blade tip clearance region (r = 0.99) at three flow rates: (a) Q/Q_{des} = 0.9; (b) Q/Q_{des} = 1.0; (c) Q/Q_{des} = 1.1.

show more pronounced gradients, indicating intensified shear interactions between the tip leakage flow and mainstream flow. The expansion of high-velocity zones corresponds to the more elongated TLV structure shown in Figure 7, while the enhanced velocity gradients provide the necessary momentum for the vortex trajectory extension observed in Figure 8.

Under Q/Q_{des} = 1.1, the velocity distribution reaches maximum intensity with extensive high-velocity regions spanning across the entire blade chord. The velocity gradients become steepest, creating optimal conditions for vorticity generation and TLV formation. The substantially increased streamwise extent of velocity variations directly supports the enhanced three-dimensional TLV characteristics and deeper vortex penetration into the main flow channel documented in Figure 8. Furthermore, the intensified velocity field explains the longer recirculation patterns and more complex streamline trajectories presented in Figure 9, demonstrating how the underlying velocity distribution governs the overall TLV behaviour and structural evolution.

Figure 11 presents velocity triangle diagrams at the impeller blade inlet under different flow rate conditions, where V, U, and W represent the absolute velocity, circumferential velocity, and relative velocity, respectively. Figure 11(a) shows the physical arrangement of velocity vectors on the blade geometry, while Figure 11(b) illustrates the quantitative velocity triangle variations across different flow conditions. The velocity triangles demonstrate systematic variations with increasing flow

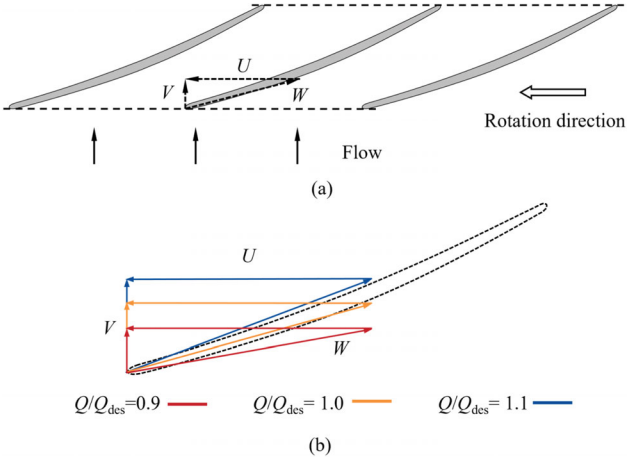

Figure 11. Velocity triangle diagrams at impeller blade inlet. (a) physical arrangement on blade geometry; (b) quantitative velocity triangles at three flow rates.

rates, directly influencing the tip leakage vortex characteristics.

As the flow rate increases from $Q/Q_{des} = 0.9$ to 1.1, the velocity triangle geometry undergoes significant changes. The relative velocity W shows a progressive increase, while the absolute velocity V magnitude grows substantially with altered flow angles. These changes result in steeper velocity triangles with larger velocity magnitudes at higher flow rates. The enhanced velocity gradients create stronger pressure differentials across the blade tip clearance, which intensify the driving force for tip leakage flow.

The evolving velocity triangle geometry directly correlates with the TLV development patterns observed in previous figures. Higher velocity magnitudes at overload conditions provide greater momentum for vortex formation, explaining the progressive transition from compact vortex structures at part-load to more complex flow patterns at overload conditions.

Figure 12 presents the distribution of time-averaged flow parameters along the blade chord in the tip clearance region under three operating conditions. The water velocity distribution (Figure 12a) reveals distinct patterns closely related to TLV formation mechanisms. At the leading edge ($\lambda = 0$), all operating conditions exhibit relatively high velocities (8–14 m/s), with $Q/Q_{des} = 1.1$ demonstrating the highest peak velocity of approximately 14 m/s. This high-velocity zone corresponds to the maximum pressure differential between the blade pressure and suction surfaces, providing the primary driving force for tip leakage flow and directly influencing TLV initial strength and formation location. A characteristic velocity drop occurs in the early chord region ($\lambda = 0.1$–0.2), corresponding to flow deceleration as the tip leakage flow adjusts to the pressure gradient. The steepness of velocity gradients in this region determines shear layer intensity, thereby controlling the initial vorticity generation rate of TLV. Combined with observations from Figs. 7 and 8, this region represents the critical location where TLV begins to deviate radially and develop toward the main flow channel. Beyond $\lambda = 0.3$, velocity profiles stabilize around 7–8 m/s across all operating conditions, coinciding with the more organized streamline regions observed in Figure 9.

The gas–liquid velocity difference distribution (Figure 12b) reveals unique mechanisms of TLV formation in multiphase flow environments. Near the leading edge ($\Delta V = -0.4$ m/s), significant negative velocity differences indicate gas phase lagging behind liquid phase due to strong liquid acceleration under high pressure gradients. This interphase velocity difference generates additional interphase shear in the TLV core region, enhancing vorticity generation and affecting the

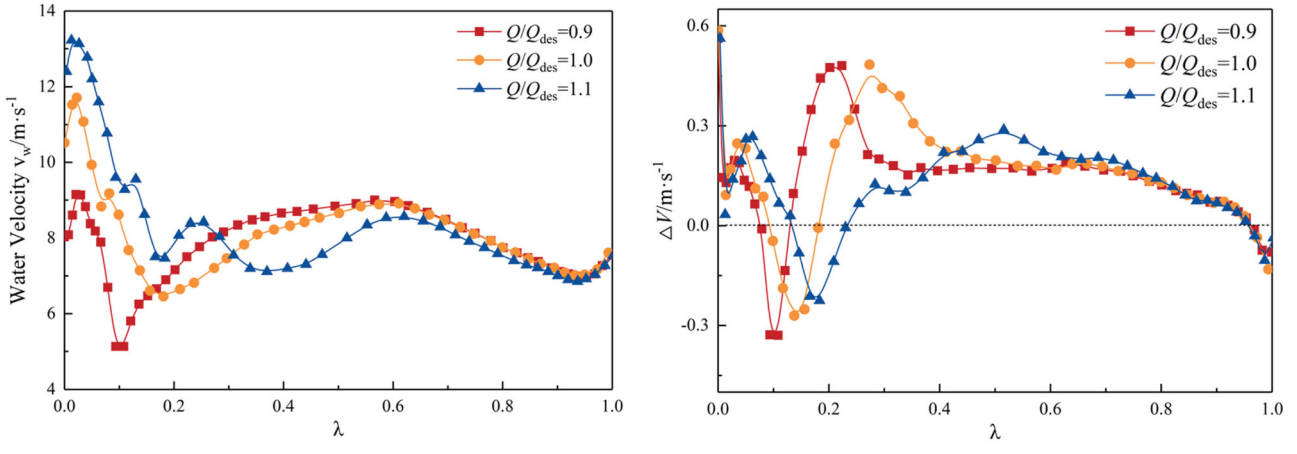

Figure 12. Chordwise distribution of time-averaged parameters in tip clearance region. (a) water velocity; (b) gas-liquid velocity difference (ΔV).

initial helical structure of TLV. In the mid-chord region ($\lambda = 0.2$–0.4), velocity differences become positive and reach peak values, suggesting gas phase acceleration exceeding liquid phase velocity, reflecting complex phase interactions under centrifugal forces and pressure gradients. The peak velocity difference in this region corresponds to the characteristic 'dip' in TLV trajectories shown in Figure 8, indicating that interphase momentum transfer directly influences vortex core radial migration behaviour. Toward the trailing edge ($\lambda > 0.6$), velocity differences gradually diminish and approach zero, indicating convergence of phase velocities and establishment of relative flow equilibrium, which affects TLV dissipation characteristics and mixing degree with mainstream flow near the trailing edge.

3.2. Flow dynamics and turbulence characteristics

Figure 13 presents contour plots of the pressure coefficient (C_p) distribution in axial sections along the blade at different chord positions under three operating conditions. The vortex core regions are visualized using Q-criterion iso-surfaces ($Q = 3 \times 10^4$), with dots marking the maximum Q values representing the actual vortex core centres. The pressure coefficient distribution reveals the characteristic low-pressure regions associated with tip leakage vortex development, where the vortex cores consistently coincide with the most negative C_p values, confirming the strong correlation between vorticity concentration and pressure depression. At $Q/Q_{des} = 0.9$, the low-pressure zones are localized and confined near the blade tip region, with the vortex cores showing

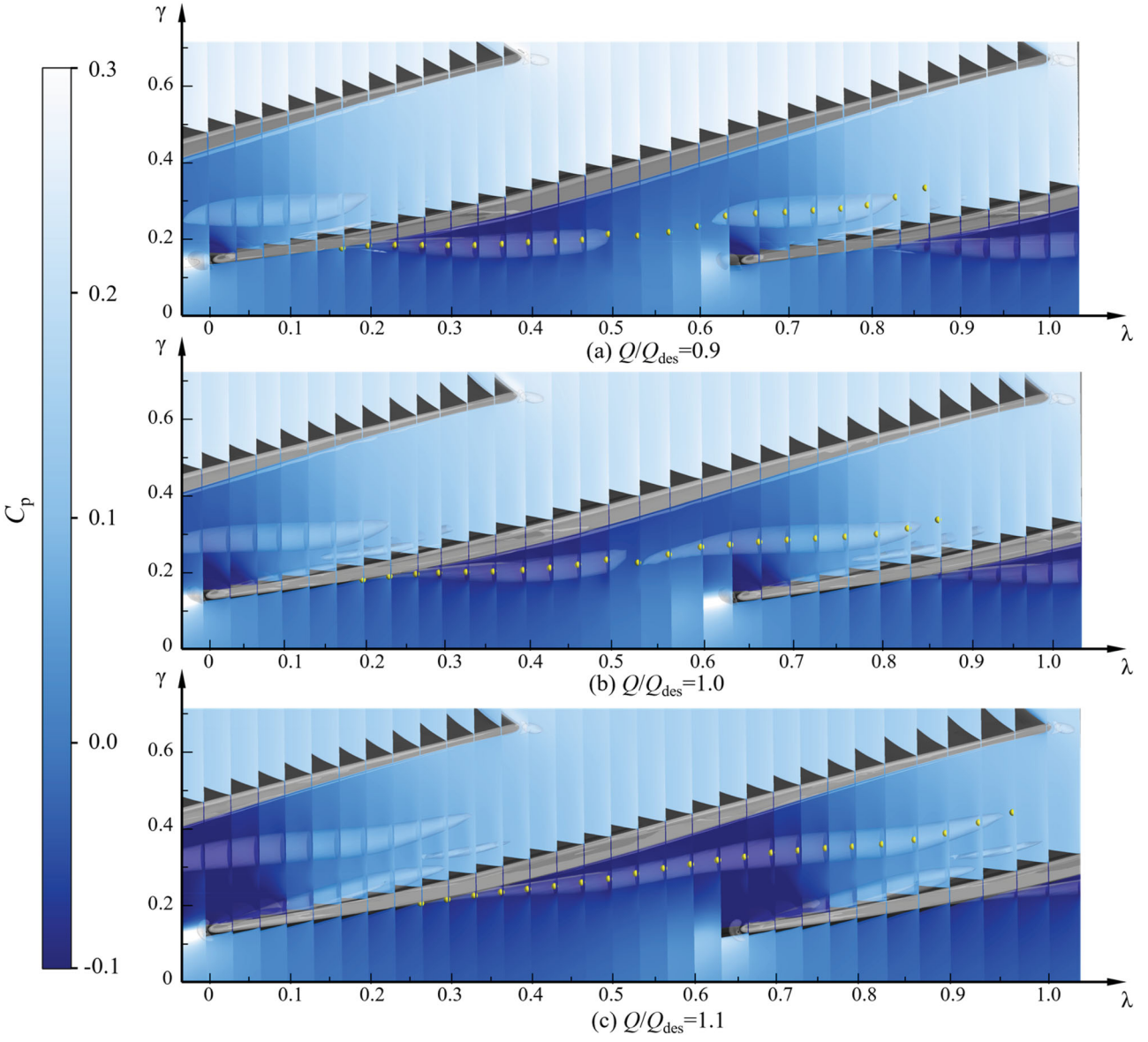

Figure 13. Pressure coefficient (C_p) contours in axial sections along the blade at different chord positions. Vortex cores visualized by Q-criterion iso-surfaces ($Q = 3\times10^4$), with dots marking maximum Q values. (a) $Q/Q_{des} = 0.9$; (b) $Q/Q_{des} = 1.0$; (c) $Q/Q_{des} = 1.1$.

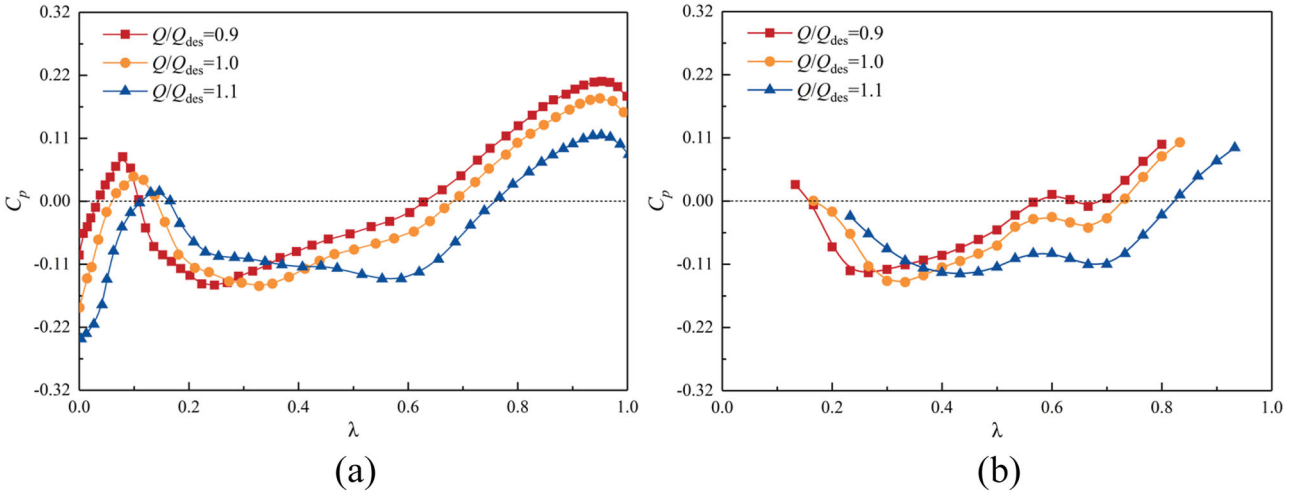

Figure 14. Chordwise distribution of time-averaged pressure coefficient (C_p) at different flow rates. (a) measured in blade tip clearance region; (b) measured at vortex core centres.

moderate intensity and limited axial extent. The pressure gradient from the vortex centre to the surrounding flow remains relatively gentle, indicating weaker vortex strength. As flow rate increases to $Q/Q_{des} = 1.0$, the low-pressure regions become more pronounced and extend further into the main flow passage. The pressure coefficient values become more negative, suggesting intensified vortex strength and enhanced momentum exchange between the tip leakage flow and the main passage flow. At $Q/Q_{des} = 1.1$, the most dramatic changes occur, with extensive low-pressure zones spanning larger portions of the blade passage and the vortex cores penetrating significantly deeper toward the hub region. The pressure coefficient distribution shows the steepest gradients and most negative values, indicating maximum vortex intensity and strongest flow interaction. The axial evolution of the vortex cores, tracked by the yellow markers, demonstrates how the TLV trajectory becomes increasingly complex and extends further downstream at higher flow rates.

Figure 14 presents the distribution of time-averaged pressure coefficient under different flow rate conditions at two distinct locations: (a) in the blade tip clearance region, and (b) at the tip leakage vortex core centres. In the tip clearance region (Figure 14a), all operating conditions exhibit a characteristic pressure recovery pattern along the blade chord, starting with relatively high pressure coefficients ($C_p = 0.1$) at the leading edge, followed by a significant pressure drop in the early chord region ($\lambda = 0.1$–0.3) where C_p reaches minimum values of approximately -0.2 to -0.3. This pressure depression zone corresponds to the high-velocity regions identified in Figure 12, confirming the strong correlation between flow acceleration and pressure reduction.

Beyond the mid-chord region ($\lambda > 0.4$), pressure gradually recovers toward the trailing edge, with higher flow rates showing less complete pressure recovery, indicating stronger flow disturbances and energy losses. The vortex core pressure distribution (Figure 14b) reveals more dramatic pressure variations, with significantly lower pressure coefficients throughout the blade chord compared to the tip clearance measurements. The vortex cores consistently maintain highly negative pressure coefficients, particularly in the mid-chord region where values reach -0.15 to -0.2, corresponding to the regions where Figure 13 showed the most intense low-pressure zones and deepest vortex core penetration. The pressure coefficient patterns in the vortex cores exhibit similar trends to the tip clearance region but with amplified magnitude, demonstrating the concentrated nature of the pressure depression within the vortex structure. Higher flow rates show progressively more negative pressure coefficients in both measurement locations, with $Q/Q_{des} = 1.1$ exhibiting the steepest pressure gradients and most severe pressure depression, correlating with the enhanced vortex strength and extended recirculation patterns observed in previous figures. The comparison between tip clearance and vortex core pressure distributions quantifies the pressure gradient that drives the tip leakage flow and sustains the vortical motion.

Figure 15 presents contour plots of vorticity magnitude in axial sections along the blade at different chord positions under three operating conditions. Magnified views (circular insets on the right) highlight the detailed vorticity structures in representative high-vorticity regions near the blade tip, with the locations marked by black circles on the main contour plots. The

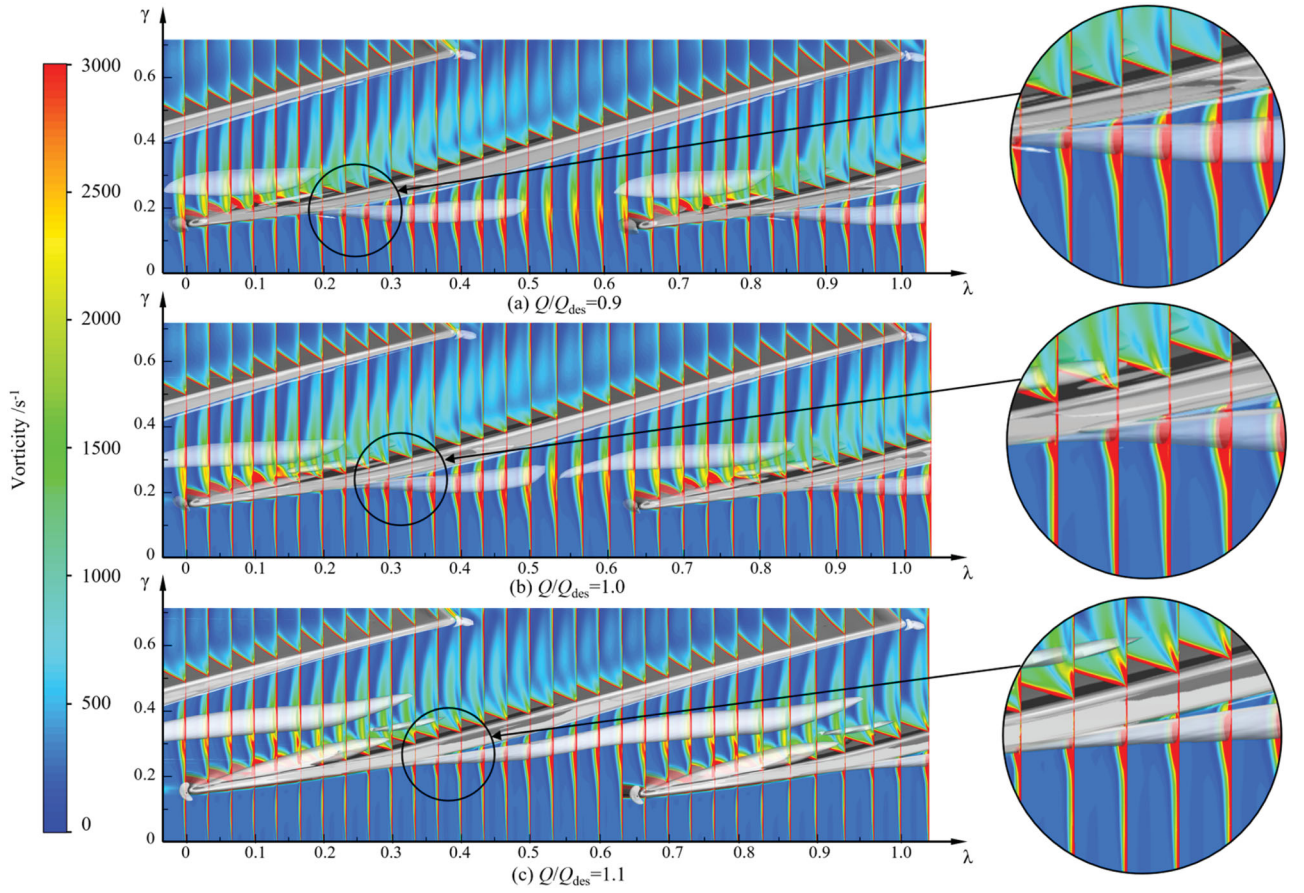

Figure 15. Vorticity magnitude contours in axial sections along the blade at different chord positions. (a) $Q/Q_{des} = 0.9$; (b) $Q/Q_{des} = 1.0$; (c) $Q/Q_{des} = 1.1$.

vorticity contours demonstrate the spatial evolution of TLV intensity. At $Q/Q_{des} = 0.9$, the vorticity distribution shows moderate intensity with peak values, primarily concentrated near the blade tip region and forming relatively compact high-vorticity zones. The enlarged view clearly reveals the localized and concentrated nature of vorticity distribution, with sharp gradients at the vortex core boundaries. As flow rate increases to $Q/Q_{des} = 1.0$, the vorticity magnitude intensifies significantly, with more extensive high-vorticity regions extending deeper into the blade passage. At $Q/Q_{des} = 1.1$, the vorticity distribution exhibits the most dramatic characteristics, with extensive regions of high vorticity spanning larger portions of the blade channel and penetrating significantly deeper toward the hub region. The vorticity patterns show remarkable spatial agreement with both the expanded low-pressure zones in Figure 14, confirming the coupled nature of vortical motion, pressure field development, and multiphase flow redistribution. The magnified insets provide detailed visualization showing that maximum vorticity values are highly localized within narrow regions near the blade tip, typically spanning only 2–3% of the blade pitch in the circumferential direction, which explains the severe flow gradients and enhanced energy dissipation in this region. The axial evolution of vorticity reveals how TLV strength and structure develop along the blade chord, with peak vorticity typically occurring in the early to mid-chord regions where pressure gradients are steepest and gas accumulation is most pronounced. The progressive increase in vorticity magnitude and spatial extent with higher flow rates demonstrates how operating conditions fundamentally control the intensity of rotational motion within tip leakage vortices.

Figure 16 presents the vorticity distribution in the tip leakage vortex core under different flow rate conditions. The overall trend analysis reveals several fundamental characteristics of TLV vorticity evolution. All three operating conditions exhibit a consistent pattern: extremely high vorticity concentrated in the leading edge region ($\lambda = 0.15$–0.25), followed by rapid exponential decay along the blade chord. This universal trend indicates that the primary vorticity generation mechanism occurs near the blade leading edge, where the pressure differential between blade surfaces is maximum and tip leakage flow acceleration is most intense.

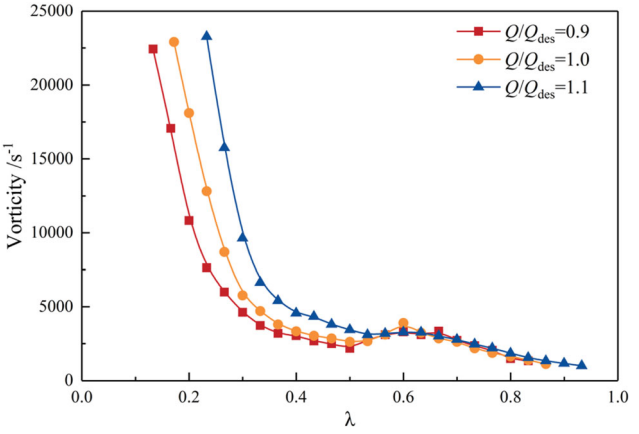

Figure 16. Vorticity distribution in the tip leakage vortex core under different flow rate conditions.

The observed vorticity decay patterns align with the theoretical framework proposed by Zhou et al. (2025), where the evolution of rigid vorticity is governed by distinct transport mechanisms. The extremely high vorticity concentration near the leading edge can be attributed to the dominance of the Vorticity Stretching Term, which controls shear vorticity generation in regions of maximum velocity gradients. The subsequent rapid decay along the chord reflects the increasing influence of viscous dissipation as the vortex structure evolves downstream. Furthermore, Zhang et al. (2025) identified that gap leakage vortices are jointly controlled by inertial stretching and rotation effects, which is consistent with our observations of sustained vorticity at higher flow rates where enhanced momentum flux provides greater resistance to dissipation.

The decay characteristics demonstrate flow rate-dependent behaviour, with higher flow rates maintaining elevated vorticity levels for extended chord distances. This sustained vorticity at overload conditions corresponds directly to the enhanced TLV structural complexity and deeper radial penetration observed in previous analyses. The vorticity decay rate becomes progressively slower as flow rate increases, suggesting that higher momentum flux in the tip leakage flow provides greater resistance to viscous dissipation and maintains rotational motion integrity over longer distances.

Figure 17 presents streamlines and turbulent kinetic energy distributions along different chord positions under three flow rate conditions. The results reveal systematic variations in flow structure and turbulence characteristics as the flow progresses from leading edge to trailing edge. At the leading edge section ($\lambda = 0.1$), the flow remains predominantly attached to the blade surface with relatively low turbulent kinetic energy concentrated near the tip region across all operating conditions. As the flow advances to $\lambda = 0.2$–0.3, turbulent kinetic energy begins to intensify, particularly for the $Q/Q_{des} = 0.9$ and $Q/Q_{des} = 1.0$ cases, with localized high-energy regions emerging near the suction side where tip leakage vortex formation initiates. The most significant turbulence development occurs in the mid-chord region ($\lambda = 0.4$–0.7), where distinct differences between operating conditions become apparent. The $Q/Q_{des} = 0.9$ case exhibits the highest turbulent kinetic energy levels, particularly at $\lambda = 0.7$, indicating enhanced flow mixing and energy dissipation under part-load conditions. Conversely, the $Q/Q_{des} = 1.1$ case demonstrates relatively lower turbulent kinetic energy levels compared to other conditions, suggesting more organized flow patterns despite higher velocity magnitudes. The red dashed lines tracking vortex core trajectories show progressive axial migration in the positive γ direction as λ increases, confirming the three-dimensional helical nature of tip leakage vortex development. The streamline patterns reveal increasingly complex recirculation zones downstream, with turbulent kinetic energy concentrated primarily in regions of large velocity gradients where tip leakage flow interacts with mainstream flow, demonstrating the fundamental relationship between vortex structure evolution and turbulence generation mechanisms.

Figure 18 presents the distribution of turbulence kinetic energy along the blade chord at different operating conditions. It shows a distinctly different pattern, with peak values occurring in the mid-chord region ($\lambda = 0.4$–0.6) rather than at the leading edge. All operating conditions exhibit maximum turbulence kinetic energy values around 1.2–1.5 m⊃2/s⊃2, with the overload condition showing slightly higher peak values and broader distribution. This downstream shift of peak turbulence relative to peak vorticity suggests that while the highest rotational motion occurs during TLV initiation, the maximum turbulent energy production occurs downstream where the organized vortical motion begins to break down and interact more chaotically with the main passage flow. The turbulence kinetic energy gradually decreases toward the trailing edge ($\lambda > 0.7$), indicating energy dissipation as the flow progresses downstream.

3.3. Phase distribution in TLV

Figure 19 presents contour plots of gas holdup distribution in axial sections along the blade at different chord positions under three operating conditions. The gas distribution reveals distinct accumulation patterns that exhibit strong spatial correlation with the low-pressure regions identified in the pressure field analysis. At $Q/Q_{des} = 0.9$, gas concentrations remain relatively

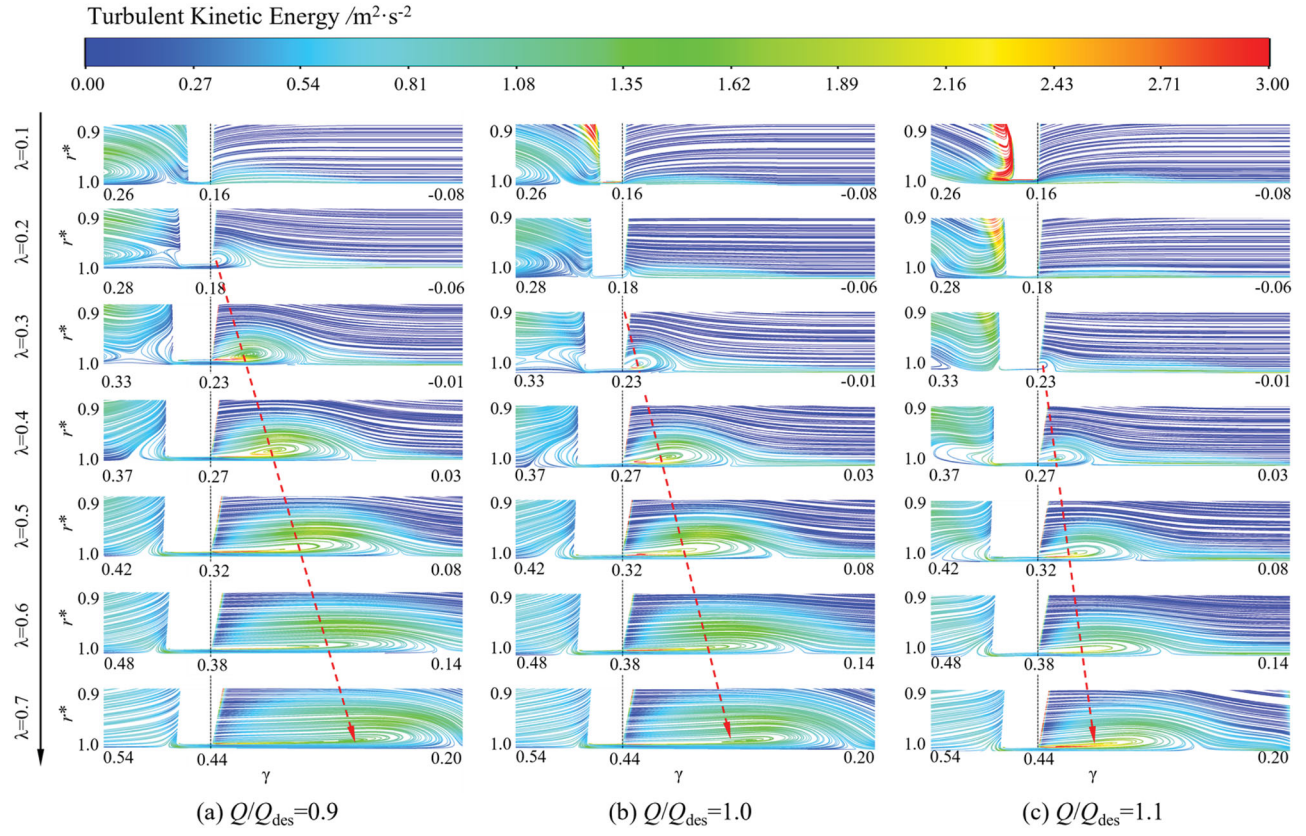

Figure 17. Streamlines and turbulent kinetic energy contours in axial sections at different chord positions (λ = 0.1 to 0.7). Red dashed lines indicate vortex core trajectories. (a) Q/Q_{des} = 0.9; (b) Q/Q_{des} = 1.0; (c) Q/Q_{des} = 1.1.

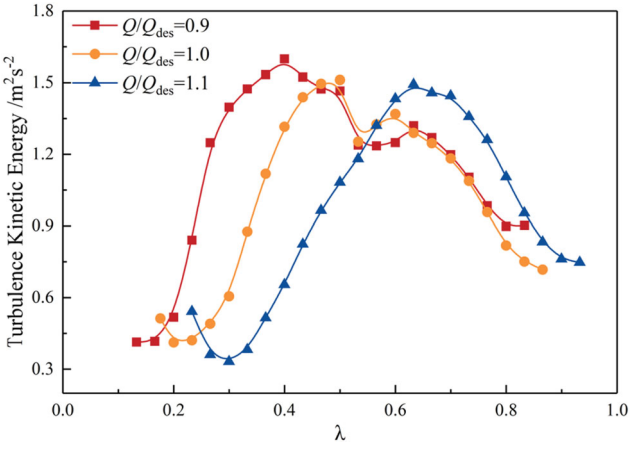

Figure 18. Distribution of turbulence kinetic energy in the axial sections along the blade at different chord positions.

localized near the blade tip and suction surface areas. These high gas concentration zones correspond precisely to the low-pressure zones identified in Figure 13, confirming the fundamental relationship between pressure depression and preferential gas phase accumulation in multiphase flows. As flow rate increases to Q/Q_{des} = 1.0, the gas holdup distribution becomes more extensive and pronounced, broader regions of elevated gas concentration extending deeper into the blade passage. The spatial extent of high gas holdup zones expands significantly, indicating enhanced gas–liquid separation under increased flow momentum. At Q/Q_{des} = 1.1, the gas holdup distribution exhibits the most dramatic characteristics, with extensive regions of high gas concentration spanning larger portions of the blade channel and penetrating significantly toward the hub region. The axial evolution of gas holdup distribution demonstrates how operating conditions fundamentally control multiphase flow structure, with higher flow rates promoting greater gas–liquid separation and more pronounced phase redistribution. The strong spatial correlation between gas holdup maxima and vortex core trajectories indicates that tip leakage vortices serve as preferential sites for gas accumulation, creating a coupled phenomenon where pressure depression facilitates gas concentration, which subsequently influences vortex stability, structural evolution, and overall multiphase flow dynamics throughout the impeller passage.

Figure 20 presents the distribution of gas volume fraction along the blade chord in the tip clearance region under three operating conditions. The results reveal distinctive phase distribution patterns that exhibit strong dependence on operating flow rates. At the leading edge,

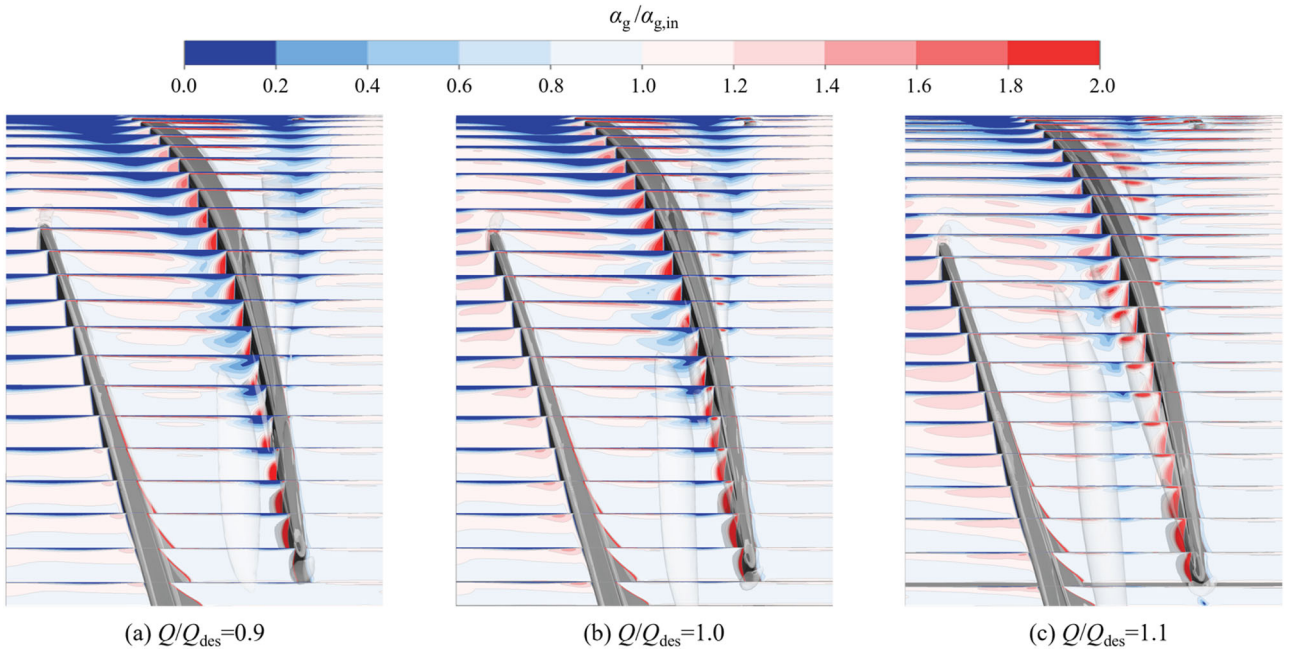

Figure 19. Relative gas holdup ($\alpha_g/\alpha_{g,in}$) contours in axial sections along the blade at different chord positions. (a) $Q/Q_{des} = 0.9$; (b) $Q/Q_{des} = 1.0$; (c) $Q/Q_{des} = 1.1$.

all operating conditions demonstrate remarkably high gas concentrations, with $Q/Q_{des} = 0.9$ exhibiting the highest peak value of approximately 0.75, while design and overload conditions reach values of 0.6–0.7. This elevated gas accumulation near the leading edge corresponds to the zone of maximum pressure differential and highest tip leakage velocity, where enhanced centrifugal effects promote gas–liquid separation. A characteristic sharp decrease in gas volume fraction occurs in the early chord region ($\lambda = 0.1$–0.2), dropping precipitously to minimum values near $\lambda = 0.3$–0.4. The inset detail view emphasizes the sharp gradient in the leading edge region. This rapid gas volume fraction variation coincides with the region of steepest velocity gradients identified in Figure 12, confirming the coupled relationship between flow acceleration and phase redistribution mechanisms.

Beyond the mid-chord region ($\lambda > 0.4$), gas volume fraction demonstrates a gradual recovery rather than continued accumulation, with values stabilizing around the inlet gas fraction of approximately 0.2 across all operating conditions. This recovery pattern indicates that the intense phase separation effects observed near the leading edge gradually diminish as the flow progresses downstream, allowing the gas–liquid mixture to approach a more equilibrated state. The trailing edge region shows relatively uniform gas distribution, suggesting that the multiphase flow achieves a more homogeneous condition as it exits the blade passage. Overall, these flow rate-dependent phase distribution patterns reveal that tip leakage vortex formation is fundamentally coupled with

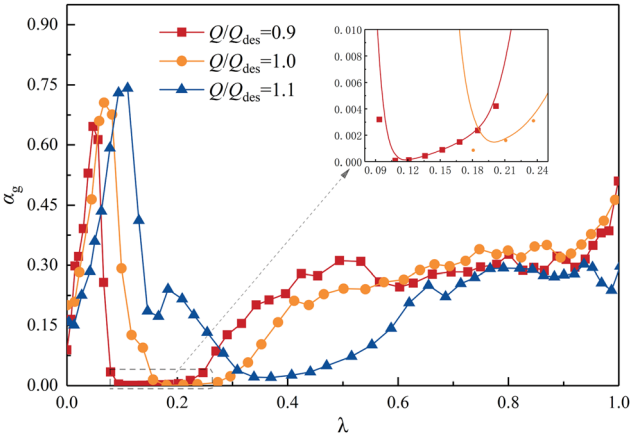

Figure 20. Chordwise distribution of gas volume fraction (α_g) in tip clearance region at three flow rates.

multiphase flow redistribution, where operating conditions control both the intensity of initial phase separation and the subsequent re-equilibration process, ultimately determining the multiphase characteristics of TLV structures throughout the blade tip clearance region.

Figure 21 presents the distribution of normalized gas holdup deviation along the blade chord at different operating conditions, where the parameter is defined as $(\alpha_g\text{-}\alpha_{g,in})/\alpha_{g,in}$, representing the degree of gas accumulation relative to the inlet conditions. The normalized gas holdup deviation reveals dramatic gas accumulation patterns that vary significantly with

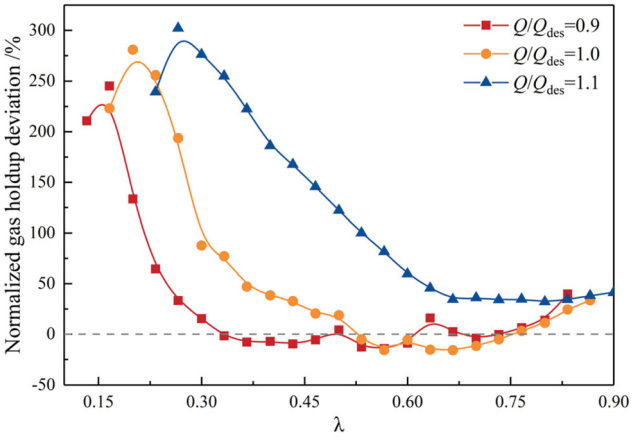

Figure 21. Chordwise distribution of normalized gas holdup deviation at three flow rates.

operating conditions and chord position. At the leading edge region ($\lambda = 0.15$–0.25), all operating conditions exhibit extremely high normalized deviations, with $Q/Q_{des} = 1.1$ showing the most pronounced gas accumulation with deviation values exceeding 300%. $Q/Q_{des} = 0.9$ demonstrates moderate gas accumulation with peak deviations around 150%, while $Q/Q_{des} = 1.0$ shows intermediate values reaching approximately 250%. This dramatic gas concentration in the leading edge region correlates directly with the high gas volume fractions confirming that the pressure depression associated with TLV formation creates preferential sites for gas phase accumulation. As the flow progresses downstream ($\lambda > 0.3$), the normalized gas holdup deviation decreases rapidly for all operating conditions, approaching near-zero or slightly negative values in the mid-chord to trailing edge regions ($\lambda = 0.45$–0.90). This transition indicates that the intense gas accumulation is primarily concentrated in the early stages of TLV development, where the pressure gradients are steepest and the vortical motion is most intense. The convergence of all curves toward minimal deviation values in the downstream region suggests that gas–liquid mixing and redistribution processes gradually restore more uniform phase distribution as the flow progresses through the blade passage.

The dramatic gas accumulation observed in the leading edge region is consistent with the gas–liquid separation mechanisms identified by Hui et al. (2024), who found that separation in helico-axial multiphase pumps occurs near 2/3 of the airfoil bone line due to asynchronous behaviour of the gas–liquid two-phase medium. The coupling between pressure depression and gas accumulation observed in our study further supports the findings of Zhou et al. (2025), who demonstrated that the Baroclinic Torque Term couples with gas–liquid density gradients to synergistically influence vortex structure. The enhanced gas–liquid separation at higher flow rates can be understood through the vorticity decomposition framework proposed by Shi et al. (2024), where the gas phase significantly increases the RCT value, contributing to prolonged TLV existence and more pronounced phase redistribution patterns.

4. Conclusions

Through numerical simulation validated by high-speed photography (maximum deviation $< 5\%$ for pressure rise, MAPE of 4.8% for efficiency), this study has comprehensively investigated tip leakage vortex characteristics and phase distribution mechanisms in helico-axial gas–liquid multiphase pumps, revealing critical coupling relationships among operating conditions, vortex dynamics, and gas–liquid phase distribution. The main conclusions and their significance are as follows:

1. As pump flow rate increases from Q/Qdes = 0.9 to 1.1, the tip leakage vortex exhibits systematic structural intensification: TLV penetration depth increases by 35%, with vortex cores migrating from $r* = 0.990$ to $r* = 0.983$ at mid-chord, representing significantly deeper intrusion into the main flow passage; recirculation zone extent increases by approximately 40% under overload conditions compared to part-load operation. These quantitative relationships establish that multiphase TLV exhibits 20–25% stronger radial migration than single-phase equivalents due to gas–liquid density stratification effects, directly impacting energy loss mechanisms.

2. Vorticity exhibits extreme spatial concentration at the blade leading edge region ($\lambda = 0.15$–0.25) with peak values exceeding 24,000 s^{-1}, followed by rapid exponential decay to below 5,000 s^{-1} by mid-chord ($\lambda = 0.5$), representing an 80% reduction over 35% chord length. In contrast, turbulent kinetic energy peaks at 1.5–1.6 m⊃2/s⊃2 in the mid-chord region ($\lambda = 0.4$–0.6), spatially offset from peak vorticity by approximately 0.2–0.3 chord lengths. The rapid vorticity decay rate is 30–40% attributed to enhanced dissipation through interphase momentum transfer. These findings indicate that turbulence-based erosion risk is highest at mid-chord rather than leading edge, requiring revised blade protection strategies.

3. Gas holdup distribution exhibits strong spatial correlation with low-pressure vortex cores: maximum gas holdup increases from 0.25 to over 0.4 (60% increase) as flow rate increases from 0.9 to 1.1 Qdes; gas volume fractions reach 0.6–0.75 near the leading edge, representing 3–3.75 times the inlet condition (20% GVF); (c) normalized gas phase deviation exceeds 300% at high

flow rates in the leading edge region ($\lambda = 0.15$–0.25). Time-averaged analysis reveals gas–liquid velocity differences reach ±0.5 m/s in TLV cores, with gas phase lagging near the leading edge then accelerating beyond liquid phase at mid-chord. The pressure-gas coupling creates a self-reinforcing degradation mechanism: pressure depression → gas accumulation → reduced liquid momentum → further pressure depression, which can trigger flow instabilities at gas fractions exceeding 25–30%.

The quantitative relationships established in this study provide actionable insights: (a) tip clearance optimization should target the leading edge region ($\lambda = 0$–0.3) where 75% of vorticity generation occurs; (b) blade surface treatments for erosion resistance should focus on mid-chord regions ($\lambda = 0.4$–0.6) where turbulent kinetic energy peaks; (c) operational flow rate should be maintained within ±5% of design point to limit gas accumulation below 250% deviation threshold that triggers instabilities.

Future research should extend this study by investigating TLV behaviour across wider gas void fraction ranges and transient operating conditions to establish comprehensive performance maps for field applications. Advanced modelling approaches such as Large Eddy Simulation combined with sophisticated experimental techniques (PIV, LDV) can provide higher-fidelity characterization of unsteady TLV dynamics, while developing vortex control strategies including optimized blade tip geometries offers potential for mitigating adverse TLV effects. The fundamental understanding of TLV-phase coupling mechanisms established in this study provides a foundation for next-generation helico-axial multiphase pump design. As offshore energy extraction moves toward deeper waters and more challenging conditions, these insights will become increasingly critical for maintaining efficient operations, with knowledge transfer potential to broader multiphase turbomachinery applications.

Acknowledgements

Yibo Gao: lnvestigation; Methodology; Software; Validation; Writing original draft. **Linlin Geng**: Methodology; Supervision; Writing-review & editing. **Patrick G. Verdin**: Writing-review & editing. **Ibra Fall**: Writing-review & editing. **Yilong Wang**: Writing review & editing. **Desheng Zhang**: Funding acquisition; Resources; Supervision; Writing-review & editing.

Disclosure statement

No potential conflict of interest was reported by the authors.

Funding

This work was supported by the National Science Foundation for Distinguished Young Scholars of China (grant number. 52425903), Jiangsu Province Science Foundation (grant number BZ2024027), NSFC Key International (Regional) Cooperation Research Project (grant number W2511051), the National Natural Science Foundation of China (grant number U2106225) and Jiangsu Provincial Frontier Technology R&D Program (grant number BF2025054).

Data availability statement

The data that support the findings of this study are available from the corresponding author upon reasonable request.

References

Celik, I. B., Ghia, U., Roache, P. J., & Freitas, C. J. (2008). Procedure for estimation and reporting of uncertainty due to discretization in CFD applications. *Journal of Fluids Engineering-Transactions of the ASME*, *130*(7), 078001. https://doi.org/10.1115/1.2960953

Drew, D. A., & Passman, S. L. (1999). *Theory of multicomponent fluids*. Springer.

Gaggero, S., Tani, G., Viviani, M., & Conti, F. (2014). A study on the numerical prediction of propellers cavitating tip vortex. *Ocean Engineering*, *92*, 137–161. https://doi.org/10.1016/j.oceaneng.2014.09.042

Ishii, M., & Hibiki, T. (2010). *Thermo-fluid dynamics of two-phase flow* (2nd ed.). Springer.

Jia, X., Gan, Z., Liu, J., Li, X., Lin, Z., & Zhu, Z. (2025). Research on the relationship between pressure pulsation and leakage vortex intensity in the blade tip clearance under various operational conditions of axial flow pumps. *Physics of Fluids*, *10*(9), 235. https://doi.org/10.3390/fluids10090235

Kim, J. H., Lee, H. C., Yoon, J. Y., Lee, K. Y., Lee, Y. K., & Choi, Y. S. (2014). Multi objective optimization of a multiphase pump for offshore plants. Paper presented at the ASME 2014 4th Joint US-European Fluids Engineering Division Summer Meeting, Chicago, Illinois, USA,https://doi.org/10.1115/fedsm2014-21206.

Liu, M., Tan, L., & Cao, S. (2018a). Design method of controllable blade angle and orthogonal optimization of pressure rise for a multiphase pump. *Energies*, *11*(5), 1048. https://doi.org/10.3390/en11051048

Liu, Y., & Tan, L. (2019). Spatial-temporal evolution of tip leakage vortex in a mixed-flow pump with tip clearance. *Journal of Fluids Engineering*, *141*(8), 081302. https://doi.org/10.1016/j.ijmultiphaseflow.2023.104445

Liu, Y., Tan, L., & Wang, B. (2018b). A review of tip clearance in propeller, pump and turbine. *Energies*, *11*(9), 2202. https://doi.org/10.21236/ad0256533

Mailach, R., Lehmann, I., & Vogeler, K. (2001). Rotating instabilities in an axial compressor originating from the fluctuating blade tip vortex. *J. Turbomach*, *123*(3), 453–460. https://doi.org/10.1115/2000-gt-0506

Menter, F. R. (1994). Two-equation eddy-viscosity turbulence models for engineering applications. *AIAA Journal*, *32*(8), 1598–1605. https://doi.org/10.2514/3.12149

Okafor, C. C., & Verdin, P. G. (2024). 3D computational fluid dynamics analysis of natural gas separation efficiency in multiphase pumping wells with heterogeneous flow regime. *Engineering Applications of Computational Fluid Mechanics*, *18*(1), 2395452. https://doi.org/10.1080/19942060.2024.2395452

Quan, H., Sun, J., Li, Y., Liu, X., Li, J., & Su, H. (2024). Research on gas–liquid separation characteristics in the helicoaxial multiphase pump. *Physics of Fluids*, *35*(11), 113304. https://doi.org/10.1063/5.0168897

Rains, D. A. (1954). *Tip clearance flows in axial compressors and pumps*. California Institute of Technology. https://doi.org/10.21236/ad0037339.

Schiller, L., & Naumann, A. (1933). A drag coefficient correlation. *Zeit. Ver. Deutsch. Ing*, *77*, 318–320. https://doi.org/10.1002/9781119283706.ch59

Shi, G., Liu, Z., Xiao, Y., Li, H., & Liu, X. (2020). Tip leakage vortex trajectory and dynamics in a multiphase pump at off-design condition. *Renewable Energy*, *150*, 703–711. https://doi.org/10.21203/rs.3.rs-1417207/v1

Shi, G., Sun, G., Wang, Q., Quan, H., Huang, Z., Wen, H., & Hao, Z. (2024). Dynamic characteristics of the tip leakage vortex in an oil–gas multiphase pump based on vorticity decomposition theory. *Energy Science & Engineering*, *12*(7), 2918–2943. https://doi.org/10.1002/ese3.1778

Shi, Q., Mao, H., & Guan, X. (2019). Numerical simulation and experimental verification of the deposition concentration of an unmanned aerial vehicle. *Applied Engineering in Agriculture*, *35*(3), 367–376. https://doi.org/10.13031/aea.13221

Suh, J. W., Kim, J. W., Choi, Y. S., Kim, J. H., Joo, W. G., & Lee, K. Y. (2018). Development of numerical Eulerian-Eulerian models for simulating multiphase pumps. *Journal of Petroleum Science and Engineering*, *162*, 588–601. https://doi.org/10.1007/s42757-019-0016-z

Tang, L., Yuan, S., Tang, Y., & Yan, H. (2018). Performance experiment and numerical prediction on the optimization design of the micro-sized water turbine for the hose reel irrigator. *International Journal of Agricultural and Biological Engineering*, *11*(5), 108–115. https://doi.org/10.25165/j.ijabe.20181105.2876

Torre, L., Pasini, A., Cervone, A., Pace, G., Miloro, P., & d'Agostino, L. (2011). Effect of tip clearance on the performance of a three-bladed axial inducer. *Journal of Propulsion and Power*, *27*(4), 890–898. https://doi.org/10.2514/1.55076

Wu, H., Miorini, R. L., & Katz, J. (2011a). Measurements of the tip leakage vortex structures and turbulence in the meridional plane of an axial water-jet pump. *Experiments in Fluids*, *50*(4), 989–1003. https://doi.org/10.1007/s00348-010-0975-0

Wu, H., Miorini, R. L., Tan, D., & Katz, J. (2012). Turbulence within the tip-leakage vortex of an axial waterjet pump. *AIAA Journal*, *50*(11), 2574–2587. https://doi.org/10.2514/1.j051491

Wu, H., Tan, D., Miorini, R. L., & Katz, J. (2011b). Three-dimensional flow structures and associated turbulence in the tip region of a waterjet pump rotor blade. *Experiments in Fluids*, *51*(6), 1721–1737. https://doi.org/10.1007/s00348-011-1189-9

Zhang, D., Shi, W., Van Esch, B. B., Shi, L., & Dubuisson, M. (2015a). Numerical and experimental investigation of tip leakage vortex trajectory and dynamics in an axial flow pump. *Computers & Fluids*, *112*, 61–71. https://doi.org/10.1016/j.compfluid.2015.01.010

Zhang, J., Cai, S., Li, Y., Zhu, H., & Zhang, Y. (2016). Visualization study of gas–liquid two-phase flow patterns inside a three-stage rotodynamic multiphase pump. *Experimental Thermal and Fluid Science*, *70*, 125–138. https://doi.org/10.1016/j.expthermflusci.2015.08.013

Zhang, J., Cai, S., Zhu, H., & Zhang, Y. (2015b). Experimental investigation of the flow at the entrance of a rotodynamic multiphase pump by visualization. *Journal of Petroleum Science and Engineering*, *126*, 254–261. https://doi.org/10.3901/jme.2015.18.184

Zhang, J., & Tan, L. (2018). Energy performance and pressure fluctuation of a multiphase pump with different gas volume fractions. *Energies*, *11*(5), 1216. https://doi.org/10.1088/1755-1315/405/1/012029

Zhang, J., Zhu, H., Yang, C., Li, Y., & Wei, H. (2011). Multi-objective shape optimization of helico-axial multiphase pump impeller based on NSGA-II and ANN. *Energy Conversion and Management*, *52*(1), 538–546. https://doi.org/10.1016/j.enconman.2010.07.029

Zhang, S., Han, W., & Li, R. (2025). Study on flow characteristics of tip clearance leakage flow in spiral axial-flow multiphase pump. *Physics of Fluids*, *37*(4), 043333. https://doi.org/10.1063/5.0266474

Zhou, J., Han, W., & Li, R. (2025). Mechanism of tip clearance leakage vortex evolution and energy loss characteristics in gas–liquid multiphase pumps based on vortex dynamics theory. *Physics of Fluids*, *37*(9), 093334. https://doi.org/10.1063/5.0287495

https://dspace.org/

Tip leakage vortex characteristics and phase distribution in a helico-axial multiphase pump at different flow rates

Gao, Yibo; Geng, Linlin; Verdin, Patrick G.; Fall, Ibra; Wang, Yilong ...

2026
Taylor & Francis
https://doi.org/10.1080/19942060.2026.2641020
Gao Y, Geng L, Verdin PG, et al., (2026) Tip leakage vortex characteristics and phase distribution in a helico-axial multiphase pump at different flow rates. Engineering Applications of Computational Fluid Mechanics, Volume 20, Issue 1, 2026, Article number 2641020

Downloaded from a DSpace repository. https://dspace.org/